Available online at www.sciencedirect.com
ScienceDirect
Journal of Catalysis 246 (2007) 249–265
JOURNAL OF CATALYSIS
www.elsevier.com/locate/jcat

High ethane dehydrogenation activity of $[GaH]^{2+}$–Al pair sites in Ga/H-[Al]ZSM-5: A DFT thermochemical analysis of the catalytic sites under reaction conditions

Yogesh V. Joshi, Kendall T. Thomson *

School of Chemical Engineering, Purdue University, West Lafayette, IN 47907, USA

Received 18 July 2006; revised 16 November 2006; accepted 26 November 2006

Abstract

Through a full thermochemical analysis at reaction conditions, we studied ethane dehydrogenation activity of extra-framework $[GaH]^{2+}$ species in Ga/H-[Al]ZSM-5 at the 6–31g(d,p)/B3LYP level. We provide a theoretical evidence to support the proposition of $[GaH]^{+}$ near-pair framework–Al sites as being the active catalytic sites for ethane dehydrogenation. Dehydrogenation activity is governed by the reducibility of $[GaH]^{2+}Z_d^{2-}$ site in the presence of H_2, which is largely dependent on a zeolite ring structure consisting of two framework Al atoms. The optimum sites are defined by the intersection of linear Brønsted–Evans–Polanyi relations between the activation energy of the structure sensitive steps and enthalpy of reduction for the catalytic site. A comparison of the carbenium and alkyl activation mechanism indicates that the activity of the alkyl activation mechanism will be limited by the removal of highly activated ($\Delta E_{act} \sim 55$–60 kcal/mol) ethene from $[HGaC_2H_5]^{+}$ species. Our thermochemical analysis also indicates that at higher temperatures, the pair–Al sites with larger Al–Al distances become more prevalent, increasing the number of optimum catalytic sites. This work suggests a potential optimal Si/Al ratio for a given Ga loading.

Keywords: Density Functional Theory; Ga–H[Al]ZSM-5; Ethane dehydrogenation; Zeolites; Brønsted–Evans–Polanyi relation; Pair–Al sites; Carbenium activation; Alkyl activation

1. Introduction

Increasing demand for hydrocarbon feedstock and a limited supply of crude oil has made nonconventional hydrocarbon resources, such as natural gas, important for future applications. Light alkane aromatization is one of the industrial processes that can use natural gas to produce value-added and easy to transport aromatics [1]. The regular mixture of the aromatics is dominated by benzene (B), toluene (T), and xylenes (X). Benzene is widely used in downstream chemical processes, such as the production of styrenes and phenols. The high octane value of toluene makes it an important gasoline additive, whereas xylenes are essential for the production of purified terephthalic acid (PTA), phthalic anhydride, and isophthalic acid. MFI (ZSM-5)-based zeolites are the preferred catalysts for the light alkane aromatization process due to their shape selectivity and lower deactivation rates. It is well known that initial dehydrogenation (activation) of light alkanes is the rate-limiting step for aromatization [1–3]. In the absence of the extra-framework metals, the initial activation is catalyzed mainly by Brønsted acid sites.

As shown in Scheme 1, alkenes can be generated by (a) protolytic dehydrogenation, (b) protolytic cracking, or (c) hydride transfer. Of these three paths, protolytic cracking and hydride transfer redistribute hydrogen to smaller alkanes and hence lower the selectivity of the unmodified HZSM-5 catalysts. It is well documented that protolytic dehydrogenation and protolytic cracking occur via the Haag–Dessau mechanism [4] with pentacoordinated carbonium ion intermediates. Activation barriers for both pathways [5] are similar, limiting the overall dehydrogenation selectivity of the Brønsted acid site. Hence, additional dehydrogenation activity in the form of extra-framework met-

---

* Corresponding author. Fax: +1 765 494 0805.
E-mail address: thomsonk@purdue.edu (K.T. Thomson).

0021-9517/$ – see front matter © 2006 Published by Elsevier Inc.
doi:10.1016/j.jcat.2006.11.032

$$C_nH_{2n+2} \xrightarrow{H^+} C_nH_{2n} + H_2 \qquad \text{(a)}$$

$$C_nH_{2n+2} \xrightarrow{H^+} C_{n-m}H_{2(n-m)} + C_mH_{2m+2} \qquad \text{(b)}$$

$$C_nH_{2n+2} + C_mH_{2m} \xrightarrow{H^+} C_nH_{2n} + C_mH_{2m+2} \qquad \text{(c)}$$

Scheme 1. Different pathways to generate unsaturation in an alkane using HZSM-5: (a) protolytic dehydrogenation; (b) protolytic cracking; (c) hydride transfer.

als, such as Ga [6,7] and Pt, is needed to improve this catalyst. The use of extra-framework metals such as Zn, In, and Cu to promote the dehydrogenation activity has also been reported in the literature [8].

To further improve these catalysts, it is necessary to understand the role of the extra-framework species. Numerous experimental investigations of Ga-promoted aromatization have been reported and reviewed [7,9–11]; however, the exact nature and role of the extra-framework Ga in the dehydrogenation reaction remains unclear. Initially it was believed that the gallium oxide is the active catalytic species, because it is capable of dehydrocyclization [12–14] and H_2 dissociations [15,16]. However, it was found that the intrinsic dehydrogenation activity of Ga_2O_3–HZSM-5 is better than that of Ga_2O_3 alone. The decrease in the activity of Ga_2O_3–HZSM-5 on the exchange of Brønsted protons with Na^+ lead to the conclusion that this catalyst operates via a bifunctional mechanism [17]. In the mechanism proposed by Meriaudeau and Naccache [17], the Ga–O coordination from oxide phase activates the C–H bond, and the alkoxide species is exchanged with a Brønsted acid site. Eventually, both H_2 and alkene desorb to regenerate the active sites. Several other studies [18–20] have proposed bifunctional mechanisms; these differ with respect to the details of the mechanistic steps and the structure of the active site. Iglesia et al. [19] inferred that the Ga species are responsible only for recombinative desorption of the surface hydrogen and pointed out the required synergism between the Brønsted and the Lewis acid site. Gnep et al. [20] proposed that the Ga sites and the Brønsted sites work independently, with Ga carrying out dehydrogenation while regular Brønsted acid sites catalyze oligomerization, β-scission, and cyclization steps. The bifunctional mechanism was further supported by Kwak and Sachtler [21], who located an optimum $[Ga]/([Ga] + [H^+])$ ratio for both activity and selectivity in Ga–HZSM-5. A hydrogen back-spillover phenomenon [22] has been proposed to support the ability of Ga species to remove H_2 from the distant Brønsted sites.

Many experimental investigations have attempted to elucidate the structure of the active site. Price et al. [23] proposed that the active catalyst is in its reduced state by observing the correlation between the extent of reduction and aromatization activity of the Ga–H/Na-ZSM-5. Using in situ Ga K-edge X-ray adsorption spectroscopy, Meitzner et al. [24] showed that for catalysts under the working conditions, the nature of the active Ga species is GaH_x. This was further confirmed by recent work from Kazansky et al. [25,26] using DRIFTS and by Hensen et al. [27] using XANES. Kazansky et al. [25] showed that the characteristic Ga–H bond stretching frequency indicates the heterogeneity of GaH_x species on the catalyst surface. The Ga–H stretching band showed decreased intensity after evacuation at the higher temperature. These authors also have pointed out that the reduced Ga^+ species is capable of activating ethane to from $[HGaC_2H_5]^+$ species [26]. Based on HRTEM-EDX results, Nowak et al. [28] proposed that a pair–Al site is an active site, where extra-framework Ga and a Brønsted acid site act in synergy.

The complexity of the propane aromatization reaction mechanism [29] necessitates the use of theoretical methods to study individual reaction steps [30–33]. Nascimento and coworkers [34–36] have observed a systematic decrease in activation energy for larger and branched hydrocarbon molecules. They also eliminated the possibility of activity enhancement due to framework-substituted Ga in Ga-based materials [36]. Few theoretical investigations have elucidated the reaction mechanism and the nature of the active site for Ga/H-ZSM-5. Methane activation on $[Ga{=}O]^+$ species was studied by Himei et al. [37] and Broclawik et al. [38]. There have been attempts to determine the active site structure based on the increased H/D exchange activity in the presence of the extra-framework Ga [39,40]. Frash and van Santen [41] considered a similar gallium site to study the ethane dehydrogenation reaction pathway. The authors classified the reaction paths as of two types: (a) a “carbenium activation” pathway consisting of an alkoxide-like intermediate along the reaction path after the activation of the C–H ($R^{\delta+}$–$H^{\delta-}$) bond, and (b) an “alkyl activation” pathway supporting the formation of Ga–C coordination after the activation of the C–H bond ($R^{\delta-}$–$H^{\delta+}$). They concluded that the alkyl activation path for the $[GaH_2]^+$ species is the least activated path for dehydrogenation. As pointed out previously [33], the large barriers of alkene desorption from Ga–alkyl species will limit the intrinsic rate of dehydrogenation [41]. Recently, an extra-framework Ga^+ site was proposed to be an active site with an alternate path for simultaneous ethene and H_2 desorption to regenerate the active site ($Ga^+Z_m^-$), with a reported activation barrier of 53.5 kcal/mol [42,43]. Although the overall activation barrier is lower than that proposed for $[GaH_2]^+Z_m^-$, it is still difficult to reconcile the differences between the experimental (39 kcal/mol) [44] and theoretical observations using an active site involving single-framework Al (Z_m).

Previously, we showed that the framework Al–pair sites (Z_d) with an extra-framework $[GaH]^{2+}$ are important for explaining the dehydrogenation activity of Ga/H-ZSM-5 [33]. We have found that the stability and hence the activity of the pair sites depends on Al–Al distance, and the calculated energetics for these sites conforms to the Sabatier principle [33]. Our results on the single-step dehydrogenation mechanism are in agreement with those reported by Pereira and Nascimento [45]. Rozanska et al. [46] used periodic density functional theory (DFT) calculations to study several pair–Al site structures and suggested novel pathways for dehydrogenation.

Our calculations have shown that the stable catalytic sites show a high barrier for initial C–H activation [33]. At the same time, we observed that if the catalytic site is very active (less stable), then regeneration of the active site at the end of the catalytic cycle becomes very difficult. In this paper, we extend this simple idea by considering an additional active site structures from Ga/H-ZSM-5 to find more robust Brønsted–Evans–Polanyi relationships [47]. The notion that less-than-optimal coordination with zeolite lattice leads to the activity of the extra-framework cations has been actively pursued in the recent literature [48–52] based on theoretical methods. However, most of these studies have assumed the activity of the site equivalent to its stability, which in turn could be calculated as the heat of a certain reaction involving the active site. In this contribution, we have quantitatively studied activity by rigorously calculating the activation barriers for the complete catalytic cycle. It has been shown that under experimental conditions, the nature of the working catalyst can be completely different than that perceived at room temperature [24]. Due to the endothermicity of the initial activation, reactions such as propane aromatization are carried out at higher temperatures (about 500 °C). Hence, for this particular system, the use of thermochemistry is very important when interpreting the results of the quantum chemical calculations.

We have used electronic DFT and thermochemical analysis to study the dehydrogenation mechanism catalyzed by $[\mathrm{GaH}]^{2+}\mathrm{Z}_d^{2-}$ sites in the Ga/H-ZSM-5. We have studied two different reaction paths for ethane dehydrogenation using pair–Al sites. Each reaction path comprises two important mechanistic parts. Initially, ethane undergoes C–H activation by either carbenium activation or alkyl activation. After desorption of ethene, removal of the molecular hydrogen is the important final reaction step to complete the catalytic cycle. We have studied both mechanistic transformations for six different structural representations of the active site from ZSM-5 lattice. Based on these calculations, we can explain various experimental observations [21,24–26,53]. The important part of this study is the application of the thermochemistry, which allows us to compare the activities of different catalytic sites under the reaction conditions.

The rest of the paper is organized as follows. In Section 2, we describe the details of the calculations, including the discussions regarding all of the cluster models, their selection, and details of the theory. In Section 3, we present results and discussions, along with the energetics of both dehydrogenation mechanisms (carbenium and alkyl activation, followed by hydrogen removal). We draw a qualitative comparison between these competing mechanisms discussed in light of our thermochemical analysis. In Section 4, we summarize our conclusions.

2. Details of the calculations

2.1. Cluster models

The MFI framework of ZSM-5 contains 12 symmetrically nonequivalent T sites. An isoelectronic substitution of the framework Si by Al requires the inclusion of charge-compensating extra-framework cations. Such framework substitution leads to the loss of symmetry, and all 96 T sites in a unit cell become nonequivalent. Electronic structure calculation of such a large unit cell becomes computationally prohibitive; thus, we have resorted to a cluster approximation.

In this contribution, we have used five distinct cluster geometries for representing the different framework structures (mainly rings) from ZSM-5. All of these clusters are prepared from the ZSM-5 crystal structure as reported by Koningsveld et al. [54]. Different T sites and the bridging oxygen atoms belonging to the main ring structure of the clusters are listed in Table 1. The clusters are named with the following convention: "Xny," where n is the number of T sites in the ring structure (not in the complete cluster) and *y* designates different possible ring structures with the same number (*n*) of T sites. "X" can take values "S" (straight channel), "Z" (zigzag channel), or "I" (intersection of two). Similar nomenclature was used by Prof. Bell's group [55,56] when studying the stability of the divalent cations in ZSM-5.

For each ring structure, there are many possible combinations for carrying out Al–pair substitutions; for example, in case of the 8-membered ring (Z8), two combinations of the framework Al substitutions (Z8a and Z8b) are studied. The number of substitutions are limited by the Loewenstein's rule [57], which forbids the Al substitution at the nearest-neighbor position to another framework Al. The symmetry of the cluster is also important in determining the unique combinations of the framework substitutions. For example, in the 4-membered ring (site Z4a in Fig. 1a), both possibilities of substitution are equivalent due to symmetry ($\mathrm{C_s}$ point group) of the cluster. As shown in Table 1, we used six different cluster models to represent pair framework–Al sites. For each cluster, a charge-compensating $[\mathrm{GaH}]^{2+}$ species was placed between the two tetrahedral framework Al. Further details about the geometry and properties of each active site are discussed in the next section. All of the clusters have Si–H terminations with fixed bond lengths of 1.4979 Å (the computed bond distance for free $\mathrm{SiH_4}$ using the equivalent level of theory). The terminal Si and H atoms were then held fixed at their initial Cartesian positions for all subsequent calculations.

$$[\mathrm{GaH}]^{2+}\mathrm{Z}_d^{2-} + \mathrm{H}_{2(\mathrm{g})} \rightarrow [\mathrm{GaH}_2]^{+}\mathrm{Z}_m^{-}\text{–}\mathrm{H}^{+}\mathrm{Z}_m^{-}. \tag{1}$$

To compare all of these catalytic site structures, we envision a simple reduction of the catalytic site as shown by reaction (1). Each gallium monohydride ($[\mathrm{GaH}]^{2+}\mathrm{Z}_d^{2-}$) site can be reduced by molecular hydrogen to generate a Brønsted acid proton ($\mathrm{H}^+\mathrm{Z}_m^-$) and a gallium dihydride ($[\mathrm{GaH}_2]^+\mathrm{Z}_m^-$), each located next to the framework Al from the pair site. We assume that the energy of the interaction between the Brønsted acid site and the $[\mathrm{GaH}_2]^+\mathrm{Z}_m^-$ is negligible compared with the reduction energy of the $[\mathrm{GaH}]^{2+}\mathrm{Z}_d^{2-}$ site. This allows us to set a common reference energy for comparing the stability of all sites in terms of the heat of reduction ($\Delta H^0_{\mathrm{red}}$). For each GaH site, multiple pathways are possible for carrying out reduction by adding H_2 across different Ga–O coordinations; for example, a Z4a site can be reduced in at least two different ways. Heterolytic addi-

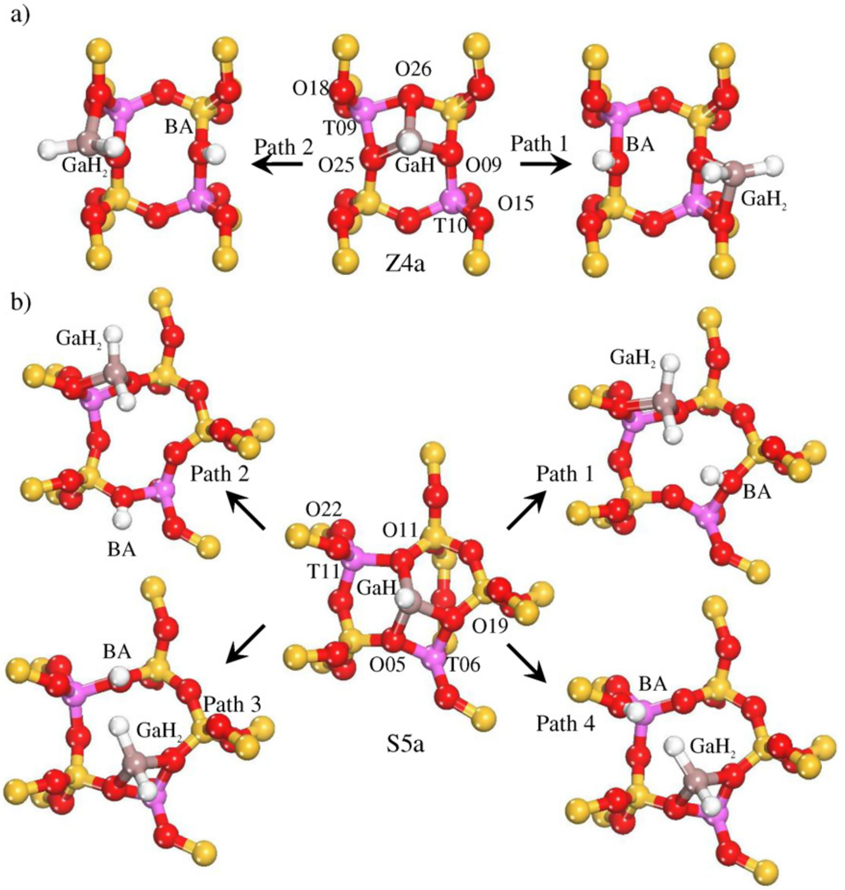

Fig. 1. Reduction pathways of $[GaH]^{2+}Z_d^{2-}$ sites: (a) two pathways (paths 1 and 2) for 4-membered ring cluster Z4a; (b) four pathways (paths 1–4) for 5-membered ring cluster S5a.

tion of hydrogen across Ga–O25 (Fig. 1a) leads to the formation of the $[GaH_2]^+$ species associated with the Al at the T10 position and the Brønsted acid site associated with the Al at the T09 position. Similar addition across the Ga–O09 coordination leads to the Brønsted acidity associated with T10 and $[GaH_2]^+$ species associated with the T09.

2.2. Theory details

For all of our calculations, we used a Becke three-parameter [58] hybrid exchange functional, along with a Lee, Yang, and Parr correlation functional [59] (B3LYP). The calculations were done using a 6-31g(d,p) double-zeta basis set [60]. With the focus of the study on the activity of the catalytic site, the contribution of the BSSE to the reaction energies and activation barriers is expected to be very small and thus is neglected. All of our calculations were done using the Gaussian03 software package [61]. For both the stable intermediates and the transition states, default convergence criteria of 0.00063 Å for an average displacement and 0.35 kcal/Å for an average gradient were used. This convergence criterion (0.00063 Å × 0.35 kcal/Å = 0.00022 kcal) is very stringent in the light of the assumptions and approximations involved in the cluster calculations; however, it ensures reproducibility and reliability for future extensions.

2.3. Cluster details

2.3.1. 4-membered ring cluster: Z4a

On relaxation, the Ga is coordinated to three of the four oxygen atoms from the Z4a ring (Fig. 1a). As reported in Table 1, the Al–Al distance is the smallest of the structures studied. The $[GaH]^{2+}$ species is located well out of the plane of the Z4a ring, to accommodate the Ga–O coordination in the small ring. As mentioned previously, there are two possible ways of reducing this monohydride site using molecular hydrogen. The heats of reduction (ΔH^0_{red}) are −7.4 and −9.5 kcal/mol. The exothermic heat of reaction indicates that the Z4a ring provides less than the optimum coordination for the extra-framework $[GaH]^{2+}$ species. Comparing the Al–Al distance before and after the reduction reveals that the Al–Al distance decreases by ∼0.2 Å on reduction. This clearly indicates that the Al–Al distance is smaller than optimal, which forces the $[GaH]^{2+}$ to push them apart. After reduction, the Brønsted acid site and $[GaH_2]^+$ have mutually independent coordination, causing the framework Al to move closer to each other in the absence of strain pushing them apart.

2.3.2. 5-membered ring cluster: S5a

This particular ring structure is located along the wall of the straight channel. The cluster consists of 15 T sites, out

Table 1
Different clusters representing the various ring structures in ZSM-5. The Al-substituted framework T positions are underlined

Cluster name	T sites	Bridging oxygens	Point group	$d_{\text{Al–Al}}$[a]	q_{Ga}[b]	Paths[c]	$d_{\text{Al–Al}}$[d]	q_{Ga}[e]	ΔH^0_{red}[f]	ΔG^0_{red}[f]
Z4a	$\underline{10}$ 10 $\underline{09}$	26 09 25	C_s	4.537	0.729	1	4.356	0.416	−7.4	−0.1
	09	09				2	4.382	0.405	−9.5	−2.3
S5a	$\underline{06}$ 05 $\underline{11}$	05 14 11	C_1	4.820	0.795	1	4.780	0.408	22.9	29.6
	12 03	20 19				2	4.660	0.428	9.4	15.9
						3	4.876	0.441	22.2	28.8
						4	4.694	0.483	16.2	23.3
S6a	$\underline{11}$ 07 07	22 23 22	C_s	4.529	0.777	1	4.636	0.508	27.9	35.3
	$\underline{11}$ 12 12	11 24 11				2	4.79	0.487	30.3	37.7
S6b	$\underline{07}$ 08 02	07 13 01	C_1	4.327	0.606	1	4.630	0.441	19.1	25.7
	$\underline{01}$ 05 11	21 14 22				2	4.477	0.437	20.5	26.5
						3	4.524	0.431	20.1	26.7
						4	4.656	0.432	21.1	27.5
Z8a	$\underline{12}$ 03 04	20 03 17	C_s	4.603	0.644	1	4.826	0.427	−3.6	3.8
	$\underline{07}$ 07 04	23 17 03				2	4.807	0.439	−3.9	3.6
	03 12	20 24								
Z8b	$\underline{12}$ 03 04	20 03 17	C_s	5.534	0.592	1	5.793	0.428	−19.6	−11.4
	07 $\underline{07}$ 04	23 17 03				2	5.790	0.442	−18.8	−10.4
	03 12	20 24								

[a] Al–Al distance in Å before reduction.

[b] Mulliken charge on the Ga before reduction.

[c] Different reduction paths for the reaction $[\text{GaH}]^{2+}\ \text{Z}_d^{2-} + \text{H}_2 \Leftrightarrow [\text{HGaH}]^+\text{Z}_m^-\text{–H}^+\text{Z}_m^-$.

[d] Al–Al distance in Å after reduction.

[e] Mulliken charge on the Ga after reduction.

[f] Heat of reduction for the reaction $[\text{GaH}]^{2+}\text{Z}_d^{2-} + \text{H}_2 \Leftrightarrow [\text{HGaH}]^+\text{Z}_m^-\text{–H}^+\text{Z}_m^-$ at 298.15 K and 1 atm.

of which positions T06 and T11 were selected for Al substitution. This particular combination was selected so that the extra-framework species have a better coordination with the framework oxygen atoms. Gallium from the $[\text{GaH}]^{2+}$ species is coordinated with three oxygen atoms from the S5a ring. There are at least four possible reduction pathways starting from the $[\text{GaH}]^{2+}\text{Z}_d^{2-}$ species. The four possible products of heterolytic addition of hydrogen across various Ga–O coordinations are shown in Fig. 1b. The heats of reaction for these pathways show large variation—from as low as 9.4 kcal/mol to as high as 22.9 kcal/mol (see Table 1). The endothermic heat of reduction indicates that the 5-membered ring provides better coordination for the $[\text{GaH}]^{2+}$ species. The near-tetrahedral coordination of the Ga in $[\text{GaH}]^{2+}\text{Z}_d^{2-}$ could be one reason for this extra stability. The Al–Al distance changes slightly after reduction depending on the reduction pathway.

2.3.3. 6-membered ring clusters: S6a and S6b

As shown in Fig. 2 we studied two types of 6-membered rings (S6a and S6b). Both rings are located along the straight channel. S6a is made up of T11, T07, T07, T11, T12, and T12, with Si at both T11 positions replaced by Al. S6b consists of T07, T08, T02, T01, T05, and T11 positions. For S6b, we substituted framework Si at the T07 and T01 positions by Al. The clusters representing S6a and S6b rings consist of 10 and 11 T sites, respectively. For both of the 6-membered rings, the $[\text{GaH}]^{2+}$ species are located at the center of the ring and are well coordinated with the four oxygen atoms. Both of the 6-membered rings offer better coordination of the monohydride species compared with the other ring structures presented here. For the S6a site, two pathways are available for carrying out the reduction. Heats of reaction for the addition of H_2 across Ga–O22 and Ga–O11 coordinations (see Fig. 2a) were 27.9 and 30.3 kcal/mol, respectively. The highly endothermic heat of reduction (ΔH^0_{red}) suggests that the site is very stable in the monohydride form.

Although for S6b structure there are at least 4 distinct reduction products (see Fig. 2b), each of these products differs in terms of the coordination of the Brønsted proton and the $[\text{GaH}_2]^+$ species. The heats of reaction for heterolytic addition of the hydrogen across Ga–O22, Ga–O21, Ga–O07, and Ga–O01 were 19.1, 20.5, 20.1, and 21.1, respectively. Compared with the S5a site, a smaller variation in the heats of reduction was observed for both of the S6 structures. This arises from the symmetric coordination of the Ga-monohydride with the framework oxygen. For both of the 6-member rings, the Al–Al distances increase (see Table 1) on reduction.

2.3.4. 8-membered ring clusters: Z8a and Z8b

The elongated 8-membered ring is composed of two 5-membered rings connected via bridging oxygen atoms. This ring

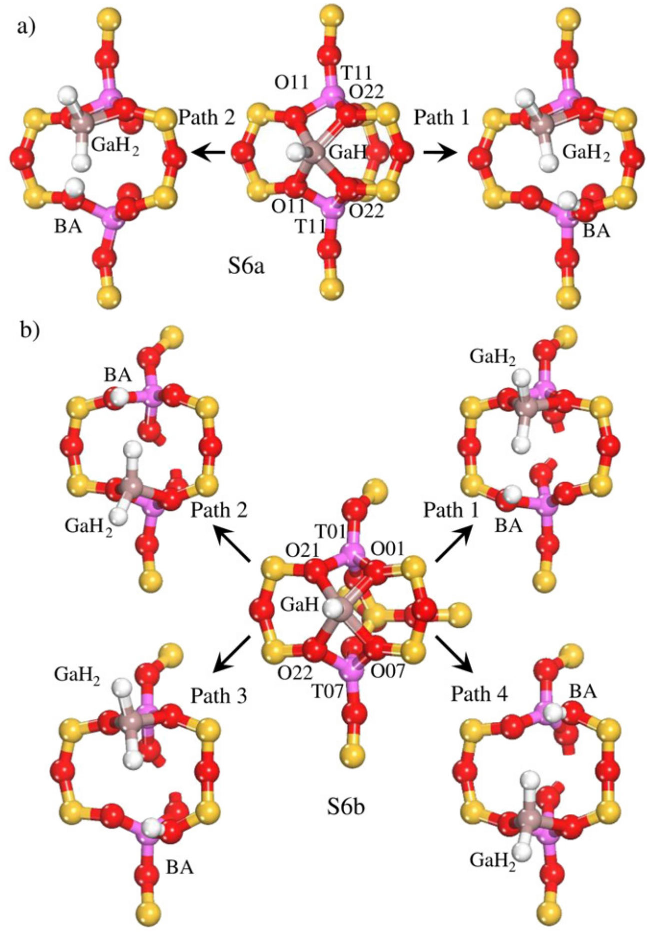

Fig. 2. Reduction pathways of $[\mathrm{GaH}]^{2+}\mathrm{Z}_d^{2-}$ sites: (a) two pathways (paths 1 and 2) for 4-membered ring cluster Z4a; (b) four pathways (paths 1–4) for 5-membered ring cluster S5a.

structure is located along the sinusoidal channel and consists of the T12, T03, T04, T07, T07, T04, T03, and T12 tetrahedral framework positions. Each cluster structure contains a total of 14 T sites. Out of several possible combinations of pair framework substitutions, we selected only two for the current investigations. We considered framework substitution at T12 and T07 positions, giving rise to structure Z8a and Z8b. However, the resulting structures are different, as seen in Figs. 3a and 3b. In the Z8a structure, the framework Al pair is along the sinusoidal channel, and the distance between the framework Al is (4.603 Å) is larger than that of S6 clusters. In Z8b, the pair of framework Al is located across the channel surface, and the distance between the framework Al atoms (5.534 Å) is the largest among all of the structures reported here. For each of the Z8 structures, we have considered two reduction products. More details about these Z8 clusters have been reported previously [33]. As expected, the Al–Al distance increases (see Table 1) on reduction, indicating that the ring contracts in an effort to provide optimum coordination to the $[\mathrm{GaH}]^{2+}$ cation.

Previously [33], we have shown that the heat of reduction of the site decreases (more exothermic) with increasing distance between framework Al atoms. Our current investigations, including the 4-membered and 8-membered rings, suggests that the reduction is exothermic if the pair of the framework Al atoms is located in a very small or a very large ring. We find that 6-membered rings provide optimum coordination for the stability of the $[\mathrm{GaH}]^{2+}\mathrm{Z}_d^{2-}$ site. The reported free energy of reduction (see Table 1) indicates that for S5a, S6a, S6b, and Z8a, the equilibrium will favor $[\mathrm{GaH}]^{2+}\mathrm{Z}_d^{2-}$ over its reduced counterpart. For less stable sites, such as Z8b, the equilibrium will favor the reduced state ($[\mathrm{GaH}_2]^{+}\mathrm{Z}_m^{-}$ and $\mathrm{H}^{+}\mathrm{Z}_m^{-}$).

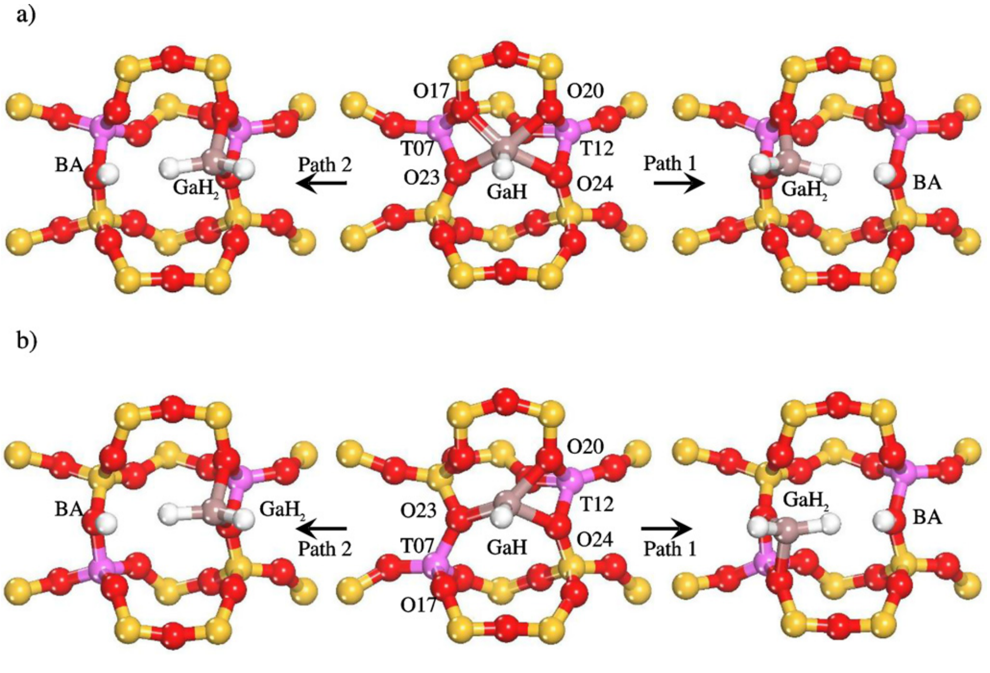

Fig. 3. Reduction pathways of $[\mathrm{GaH}]^{2+}\mathrm{Z}_d^{2-}$ sites: (a) two pathways (paths 1 and 2) for 8-membered ring cluster Z8a; (b) two pathways (paths 1 and 2) for 8-membered ring cluster Z8b.

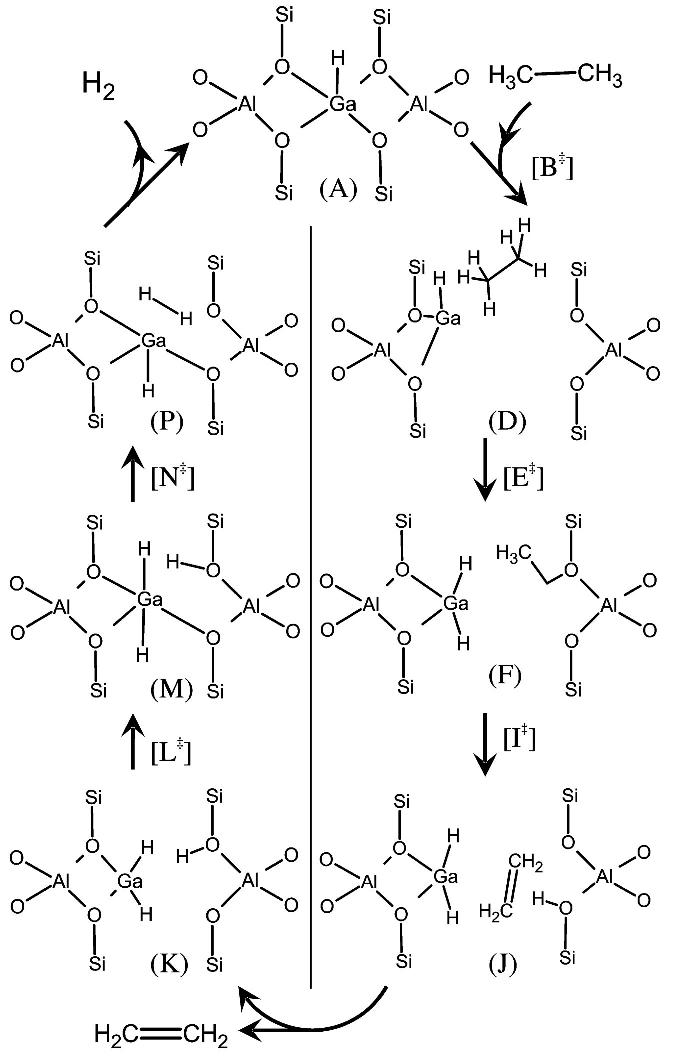

Scheme 2. Carbenium activation catalytic cycle: (A) $[GaH]^{2+}Z_d^{2-}$ site; (D) coordinatively unsaturated GaH species with ethane adsorbed “end-on”; (F) $[GaH_2]^+Z_m^-$ and $[C_2H_5]^+Z_m^-$ near respective framework Al; (J) ethene physisorbed on Brønsted acid site; (K) reduced state of the active site; (M) Ga species with higher coordination; (P) H_2 physisorbed on the coordinatively unsaturated $[GaH]^{2+}$. $B^‡$, $E^‡$, $I^‡$, $L^‡$, and $N^‡$ are the transition states for the respective mechanistic steps.

3. Results and discussions

The two basic mechanisms of C–H activation—carbenium activation and alkyl activation—are shown in Schemes 2 and 3, respectively. The carbenium activation involves C–H bond polarization in such a way that the carbon atom assumes a positive partial charge ($\delta+$) and hydrogen assumes a negative partial charge ($\delta-$). Carbenium activation leads to the formation of alkoxide and metal hydride (M–H) as an intermediate. In contrast, alkyl activation (Scheme 3) involves C–H polarization in such a way that the carbon develops a negative ($\delta-$) charge and the hydrogen develops a positive ($\delta+$) charge. Alkyl activation leads to the formation of a metal-alkyl ($M–C_nH_{2n+1}$) and the Brønsted acid as intermediates. We investigated both mechanisms for all of the clusters discussed so far, and we discuss the results next.

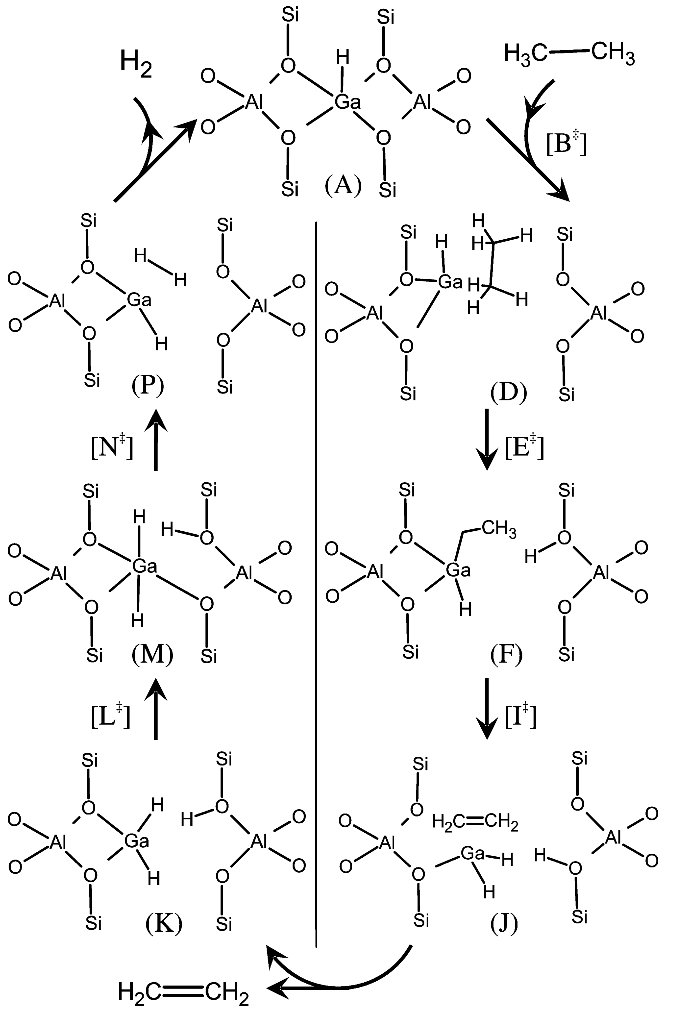

Scheme 3. Alkyl activation catalytic cycle: (A) $[GaH]^{2+}Z_d^{2-}$ site; (D) coordinatively unsaturated GaH species with ethane adsorbed “side-wise”; (F) $[HGaC_2H_5]^+Z_m^-$ and $H^+Z_m^-$ near respective framework Al; (J) ethene physisorbed on coordinatively unsaturated GaH_2; (K) reduced state of the active site; (M) Ga species with higher coordination; (P) H_2 physisorbed on the coordinatively unsaturated $[GaH]^{2+}$. $B^‡$, $E^‡$, $I^‡$, $L^‡$, and $N^‡$ are the transition states for respective mechanistic steps.

3.1. Carbenium activation mechanism

A generalized representation of the carbenium activation pathway is shown in Scheme 2. In this section, we discuss all aspects of the carbenium activation mechanism, including all of the catalytic sites studied so far. Some of the catalytic sites may show some minor deviations from the generalized scheme, which we point out. The first step involves the opening of the Ga–O coordination ($A + C_2H_6 \rightarrow [B^‡] \rightarrow D$ in Scheme 2) to form the activated intermediate D. Depending on the site geometry, the undercoordinated GaH (intermediate D), representing the activated catalytic site, may or may not be stable. The reaction coordinate for this transition mainly corresponds to the translation of the ethane toward the undercoordinated Ga. The ethane molecule is adsorbed on to the electron-deficient, coordinatively unsaturated GaH species. As was pointed out earlier, the C–H bonds of the methyl group are strongly polarized and elongated. In general, we have observed that for carbenium

Table 2
Energy barriers and reaction energies for the carbenium C–H activation ($A + C_2H_6 \rightarrow E^{\ddagger} \rightarrow F$) and ethene desorption ($F \rightarrow I^{\ddagger} \rightarrow J$) from alkoxide intermediate

Cluster	Path	$A + C_2H_6 \rightarrow E^{\ddagger} \rightarrow F$				$F \rightarrow I^{\ddagger} \rightarrow J$			
		$\Delta_C E_a$	$\Delta_C G_a^0$	$\Delta_C E_r$	$\Delta_C G_r^0$	$\Delta_{EC} E_a$	$\Delta_{EC} G_a^0$	$\Delta_{EC} E_r$	$\Delta_{EC} G_r^0$
Z4a	1	50.2	61.1	19.0	29.7	24.4	24.7	−1.2	−3.7
	2	47.7	58.5	14.2	25.0	26.8	26.8	4.6	2.1
S5a	1	75.4	85.4	51.4	61.6	19.8	20.0	−12.6	−15.0
	2	71.0	81.4	33.5	43.0	33.3	34.0	17.1	16.2
	3	81.6	92.3	48.3	58.7	21.3	21.6	−3.0	−5.3
	4	71.6	81.7	41.2	51.6	29.6	29.6	8.4	6.3
S6a	1	85.7	96.4	51.4	61.8	26.8	27.1	9.3	7.3
	2	88.6	99.2	57.4	67.8	22.4	22.6	−0.9	−3.1
S6b	1	76.8	87.0	41.3	50.5	28.4	28.9	6.0	4.9
	2	78.5	89.1	40.6	50.5	28.1	28.1	9.5	8.0
	3	77.5	88.2	42.9	53.6	28.2	27.6	8.0	5.4
	4	84.1	94.1	43.5	53.4	25.7	26.0	3.9	2.2
Z8a	1	51.7	62.6	26.9	37.8	23.5	22.7	2.6	1.8
	2	51.4	62.0	30.6	41.3	16.8	16.7	−6.4	−8.9
Z8b	1	35.0	47.7	10.5	22.1	25.1	23.9	1.9	−0.6
	2	38.4	49.2	13.8	25.5	18.8	18.6	−3.8	−7.5

Note: $\Delta_C E_a$, activation energy for carbenium activation; $\Delta_C G_a^0$, free energy barrier for carbenium activation; $\Delta_C E_r$, reaction energy for carbenium activation step; $\Delta_C G_r^0$, free energy of reaction for carbenium activation step; $\Delta_{EC} E_a$, activation energy for ethene removal from alkoxide intermediate; $\Delta_{EC} G_a^0$, free energy of activation for ethene removal from alkoxide intermediate; $\Delta_{EC} E_r$, reaction energy for ethene removal from alkoxide intermediate; $\Delta_{EC} G_r^0$, free energy change for ethene removal from alkoxide intermediate.

activation, the methyl group adsorbs in an "end-on" fashion (intermediate D in Scheme 2). In this activated intermediate, all three hydrogen atoms of the methyl group are closer to the undercoordinated Ga compared with carbon. At the same time, carbon atom is closer to the framework oxygen. These inherent steric constrains of the "end-on" adsorbed complex should lead to carbenium activation, although the electronic conditions favor alkyl activation [42].

The intermediate D further undergoes carbenium activation, as shown in Scheme 2 ($D \rightarrow [E^{\ddagger}] \rightarrow F$). This reaction step can be visualized as the S_N2 inversion of the methyl group to form an alkoxide. The coordinatively unsaturated GaH species picks up the hydrogen to generate the $[GaH_2]^+Z_m^-$ intermediate. The transition state for the S_N2 inversion has a planner $-CH_2$ group with apparent sp^2 hybridization. Transition state $E^{\ddagger}$ represents one of the highest-energy structures along the carbenium activation path. We have confirmed that the transition state $E^{\ddagger}$ is always present irrespective of the active site structures. Thus, to compare different carbenium activation paths, we define an activation energy term called the overall carbenium activation barrier ($\Delta_C E_a$). This represents the energy difference between $E^{\ddagger}$ and $A + C_2H_6$. This activation barrier represents the upper limit of the apparent activation barrier; the actual apparent activation barrier will depend on the surface coverage and hence on the reaction conditions, which can be determined via rigorous kinetic simulation [29]. We calculated the free energy change for $A + C_2H_6 \rightarrow E^{\ddagger}$ activation ($\Delta_C G_a^0$), which allowed us to compare the reaction rate along a certain reaction path and determine the rate-controlling step. For all active site structures, energy parameters related to carbenium activation are listed in Table 2. These are activation energies ($\Delta_C E_a$), free energies barriers at standard conditions ($\Delta_C G_a^0$ at 25 °C and 1 atm), reaction energies ($\Delta_C E_r$), and free energies of reaction ($\Delta_C G_r^0$).

Carbenium activation is followed by the desorption of an alkene (ethene) from the alkoxide intermediate ($F \rightarrow [I^{\ddagger}] \rightarrow J \rightarrow K + C_2H_4$), leaving behind the Brønsted acid site. As determined by our previous investigations of an alkene adsorption [30,32] on Brønsted acid sites, there are two possible mechanisms for alkene desorption: a double-site mechanism involving two framework oxygen atoms around the tetrahedral Al and a single-site mechanism involving only one framework oxygen. The double-site mechanism has two charge centers, which results in a lower activation barrier ($\Delta_C E_a$ and $\Delta_C G_a^0$). Here we discuss only the double-site mechanism and corresponding activation barriers.

As shown in Scheme 2, a double-site mechanism ($F \rightarrow [I^{\ddagger}] \rightarrow J$) would lead to ethene physisorption on the Brønsted acid site associated with the different bridging oxygen (intermediate J). However, a proton jump from one bridging oxygen to other is much more facile [62] compared with the other mechanistic steps.

In the discussions on the hydrogen desorption step that follows, we start with the Brønsted acid site on the same bridging oxygen (intermediate K) bearing the alkoxide intermediate, to be consistent with the reduction path of the $[GaH]^{2+}Z_d^{2-}$ site. The related energy parameters ($\Delta_{EC} E_a$, $\Delta_{EC} G_a^0$, $\Delta_{EC} E_r$, and $\Delta_{EC} G_r^0$) for ethene desorption are listed in Table 2. As expected, the activation barrier ($\Delta_{EC} E_a$) is fairly constant, varying around 25–35 kcal/mol. This mechanistic step is known as a "structure-insensitive reaction" in the sense that the activation barrier does not depend on the distance between the pair of the framework Al. In any case, starting from the alkoxide intermediate, the free energy of activation for alkene desorption is well

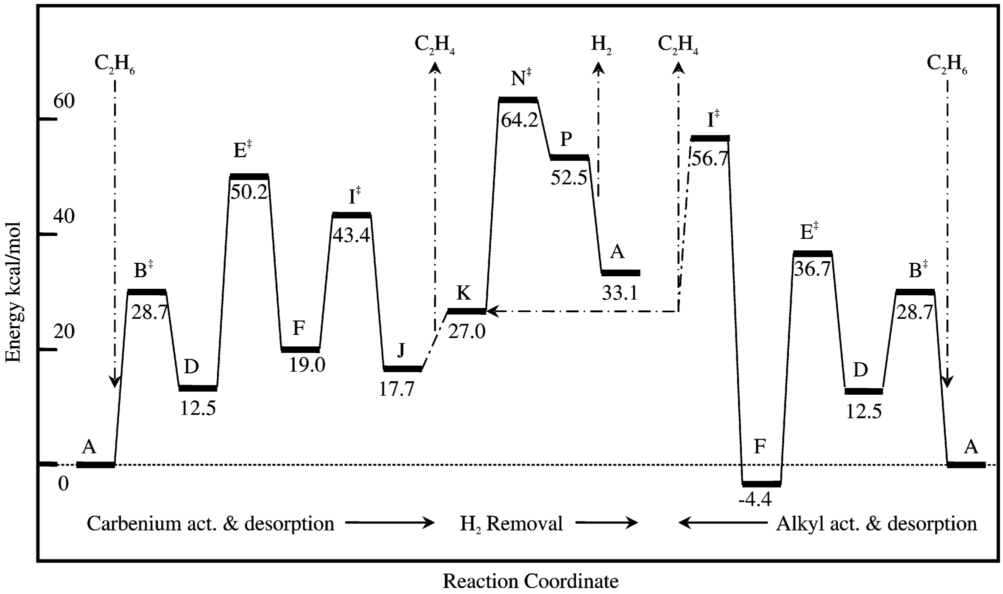

Fig. 4. Energetics of the dehydrogenation mechanism by carbenium (Scheme 2) and alkyl (Scheme 3) activation for "Z4a site pathway 1". Intermediate $L^{\ddagger}$, M along hydrogen removal path and J along alkyl activation path were not stable. Hydrogen removal energetics is common for carbenium activation and alkyl activation.

below of that for carbenium activation and thus will be inconsequential in determining the resulting apparent free energy of activation for the dehydrogenation reaction.

3.1.1. *4-membered ring cluster: Z4a*

As explained above, we considered at least two paths of heterolytic dissociation of H_2 on the Z4a site. Correspondingly, there are two carbenium activation pathways for the dissociation of C–H bond in ethane. Fig. 4 reports representative energetics for the complete catalytic cycle (both carbenium and alkyl activation; ethene and hydrogen removal) for the Z4a site. Fig. 5 reports the geometries of the reaction intermediates for this particular reaction path. The energetics for the remaining 15 reactions paths are reported in the supporting information. For the Z4a ring, the undercoordinated Ga species $[GaH]^{2+}$ lies in the plane with O–Al–O, in contrast to the more tetrahedral coordination of the Ga for the other cluster structures. At the same time, the 4-member ring presents an exception to the "end-on" adsorbed complex observed for alkyl activation. The steric repulsion of the walls surrounding the smaller ring could be a reason for the preferred "sidewise" adsorption of the ethane molecule. The overall free energies of carbenium activation ($\Delta_C G_a^0$) for the two paths for Z4a site are 61.1 and 58.5 kcal/mol. As discussed previously, for the carbenium activation mechanism, desorption of an alkene from alkoxide intermediate is much more facile with a $\Delta_{EC} G_a^0$ of 24.7 and 26.8 kcal/mol.

3.1.2. *5-membered ring cluster: S5a*

For each of the four reduction pathways for S5a, there is a distinct carbenium activation pathway. The stability of the active site in the monohydride form transpires into the higher activation energy for carbenium activation. The free energies of carbenium activation ($A + C_2H_6 \rightarrow E^{\ddagger}$, $\Delta_C G_a^0$) for four different reaction paths are 85.4, 81.4, 92.3, and 81.7 kcal/mol. The corresponding free energy barriers for ethene removal ($F \rightarrow I^{\ddagger}$ in Scheme 2) are 20.0, 34.0, 21.6, and 29.6 kcal/mol. Again, note that ethene removal from alkoxide is very facile compared with the carbenium activation mechanism.

3.1.3. *6-membered ring clusters: S6a and S6b*

The six-membered ring S6a provides the most stable coordination for the $[GaH]^{2+}$ species. Correspondingly, the highest activation barrier for the carbenium activation is observed. As noted previously [33], due to the higher stability of the catalytic site S6a in the monohydride form, the undercoordinated $[GaH]^{2+}$ species ($B^{\ddagger}$ and D) are absent along the reaction path. The free energies of carbenium activation ($\Delta_C G_a^0$) for the two mechanistic paths ($A + C_2H_6 \rightarrow E^{\ddagger}$ in Scheme 2) are 96.4 and 99.2 kcal/mol, with corresponding free energies of activation for ethene removal of ($\Delta_{EC} G_a^0$) of 27.1 and 22.6 kcal/mol.

For the other six-membered ring structure S6b, we studied four distinct carbenium activation paths. The energetics of all four reaction pathways are very similar due to symmetry of the site S6b. Because site S6b is less stable (ΔH_{red}^0 less endothermic in Table 1) than S6a, the activation barriers for carbenium activation are lower. Free energies of carbenium activation ($\Delta_C G_a^0$) are 87.0, 89.1, 88.2, and 94.1 kcal/mol. As reported in Table 2, the free energies of activation for ethene desorption are about 28 kcal/mol for all four reaction paths.

3.1.4. *8-membered ring clusters: Z8a and Z8b*

For the 8-membered ring Z8a, –3.6 kcal/mol heat of reduction indicates the formation of the $[GaH_2]^+Z_m^-$ is slightly exothermic. The lower stability of the site Z8a leads to lower free energies of the carbenium activation (62.6 and 62.0 kcal/mol for two pathways). For the other 8-membered ring Z8b, the reduction is much more exothermic with ΔH_{red}^0 of -19.6 and -18.6 kcal/mol. The least stable site shows the lowest free energy of carbenium activation ($\Delta_C G_a^0$), 47.7 and 49.2 kcal/mol.

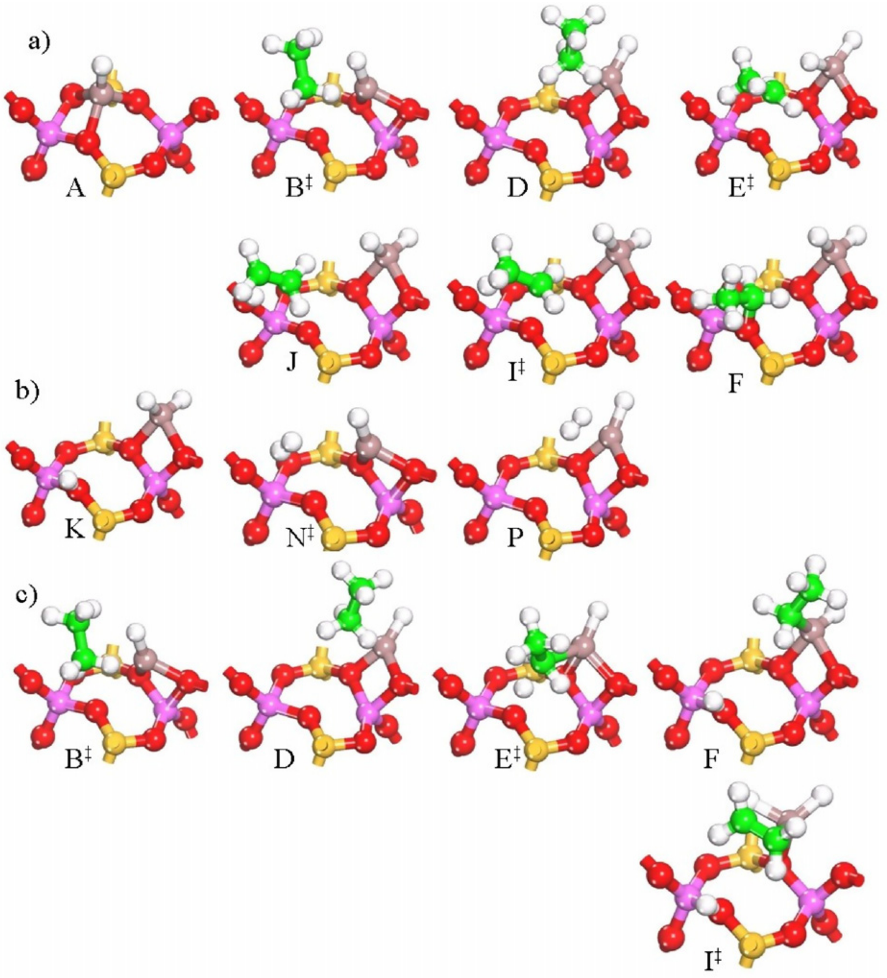

Fig. 5. Geometries of reaction intermediates for: (a) carbenium activation; (b) H_2 removal; (c) alkyl activation for “Z4a site pathway 1”.

The $\Delta_{\mathrm{EC}}G_{\mathrm{a}}^{0}$ for ethene desorption is about 22 kcal/mol, much lower than that for carbenium activation.

3.2. Alkyl activation mechanism

Scheme 3 shows a generalized catalytic cycle for dehydrogenation starting with alkyl activation, including all possible intermediates along any alkyl activation path. Not all of these intermediates may be present for a particular catalytic site, however. In our previous publication on the role of framework–Al pair sites, we specifically focused on the carbenium activation mechanism, expecting a very high activation barrier [33,41] for alkene desorption from Ga–alkyl species. Frash and van Santen [41] showed that for the active site involving single-framework–Al, alkyl activation has a lower activation barrier than carbenium activation. A similar trend is expected for the framework–Al pair sites. Similar to the carbenium activation, here the first step involves opening of the Ga–O coordination ($A + C_2H_6 \rightarrow [B^{\ddagger}] \rightarrow D$ in Scheme 3) to form the activated intermediate D. In contrast to “end-on” adsorbed complex for carbenium activation, for alkyl activation, we observed that the methyl group adsorbs in a “sidewise” fashion (intermediate D in Scheme 3). In this activated intermediate, only two hydrogen atoms and the carbon of the methyl group are closer to the undercoordinated Ga. On the opposite side of the Ga, the third hydrogen of the methyl group is closer to the framework oxygen. This C–H bond of the methyl group is strongly polarized and elongated. Thus, the geometry of the intermediate D for alkyl activation is conducive for the formation of the Ga–alkyl species and Brønsted acid site. Thus, the “sidewise” adsorbed ethane molecule should lead to the sterically controlled alkyl activation.

The intermediate D further undergoes alkyl activation as shown in Scheme 3 ($D \rightarrow [E^{\ddagger}] \rightarrow F$). The mechanistic step is seen as the S_N2 inversion of the methyl group caused by the electrophilic attack of the undercoordinated GaH species. The transition state for the S_N2 inversion has planner $-CH_2$ geometry with apparent sp^2 hybridization. Similar to carbenium activation, we found that the transition state $E^{\ddagger}$ is always present along the alkyl activation path irrespective of the structure of the catalytic site. Thus, to compare different alkyl activation paths, we have defined an activation energy term called the overall alkyl activation barrier ($\Delta_{\mathrm{A}}E_{\mathrm{a}}$), representing the energy difference between $E^{\ddagger}$ and $A + C_2H_6$. This activation barrier is the approximate apparent activation barrier, because we have neglected the possible presence of the intermediates B and $D^{\ddagger}$ for our analysis. We calculated the corresponding free energy

Table 3
Energy barriers and reaction energies for the alkyl C–H activation ($A + C_2H_6 \rightarrow E^{\ddagger} \rightarrow F$); ethene removal ($F \rightarrow I^{\ddagger} \rightarrow K + C_2H_4$) from Ga–alkyl species. Energy barriers for simultaneous ethene and H_2 removal via cyclic transition state proposed by Pidko et al. [42]

Cluster	Path	$A + C_2H_6 \rightarrow E^{\ddagger} \rightarrow F$				$F \rightarrow I^{\ddagger} \rightarrow K + C_2H_4$				Cyclic TS	
		$\Delta_A E_a$	$\Delta_A G_a^0$	$\Delta_A E_r$	$\Delta_A G_r^0$	$\Delta_{EA} E_a$	$\Delta_{EA} G_a^0$	$\Delta_{EA} E_r$	$\Delta_{EA} G_r^0$	$\Delta_{ED} E_a$	$\Delta_{ED} G_a^0$
Z4a	1	36.7	47.6	−4.4	5.0	61.1	62.0	31.4	21.1	54.0	53.9
	2	31.7	42.7	−6.6	2.9	63.5	64.4	31.4	21.1	54.1	54.2
S5a	1	55.6	66.4	25.0	34.4	55.9	56.5	32.0	21.5	52.7	52.5
	2	51.0	61.9	11.8	20.8	57.3	57.8	31.7	21.4	53.0	53.1
	3	56.3	66.6	29.3	38.6	48.5	48.8	27.0	16.5	51.6	50.8
	4	44.2	54.7	24.2	33.8	63.8	63.9	26.2	15.7	52.9	51.8
S6a	1	58.8	69.6	35.2	44.9	60.7	60.5	27.0	16.6	54.2	53.7
	2	63.2	73.8	37.2	46.8	54.1	54.7	27.4	17.1	54.4	53.7
S6b	1	54.0	64.7	24.3	33.6	62.2	62.5	28.7	18.4	55.1	55.0
	2	56.8	67.9	25.6	34.8	61.1	62.5	28.8	18.0	55.2	55.9
	3	58.3	69.3	29.7	38.7	54.8	56.5	24.4	14.2	54.3	54.9
	4	58.8	70.2	28.0	37.4	62.0	62.1	27.1	16.3	54.7	55.5
Z8a	1	32.0	42.5	2.4	11.9	63.0	63.3	28.4	18.1	54.5	54.4
	2	26.7	37.7	3.0	12.3	62.9	64.1	27.6	17.5	55.1	55.0
Z8b	1	18.0	29.0	−13.6	−3.2	65.3	65.5	28.7	18.1	54.5	54.2
	2	16.0	27.0	−11.6	−1.4	66.2	66.8	27.5	17.2	55.1	55.0

Note: $\Delta_A E_a$, activation energy for alkyl activation; $\Delta_A G_a^0$, free energy barrier for alkyl activation; $\Delta_A E_r$, reaction energy for alkyl activation step; $\Delta_A G_r^0$, free energy of reaction for alkyl activation step; $\Delta_{EA} E_a$, activation energy for ethene removal from Ga–alkyl species; $\Delta_{EA} G_a^0$, free energy of activation for ethene removal from Ga–alkyl species; $\Delta_{EA} E_r$, reaction energy for ethene removal from Ga–alkyl species; $\Delta_{EA} G_r^0$, free energy change for ethene removal from Ga–alkyl species; $\Delta_{ED} E_a$, activation energy for cyclic transition state for decomposition of Ga–alkyl species; $\Delta_{ED} G_a^0$, free energy of activation for cyclic transition state for decomposition of Ga–alkyl species.

change ($\Delta_A G_a^0$) for $A + C_2H_6 \rightarrow E^{\ddagger}$ transformation and in Table 3 report the energy terms for all of the alkyl activation paths: alkyl activation energy ($\Delta_A E_a$), standard free energies of activation ($\Delta_A G_a^0$ at 25 °C and 1 atm), reaction energy ($\Delta_A E_r$), and free energy change for alkyl activation ($\Delta_A G_r^0$).

Alkyl activation is followed by desorption of an alkene (ethene) from the Ga–alkyl intermediate ($F \rightarrow [I^{\ddagger}] \rightarrow J \rightarrow K + C_2H_4$), leaving behind the gallium dihydride species ($[GaH_2]^+Z_m^-$). Relaxation of the transition state $I^{\ddagger}$ toward product leads to the formation of the intermediate J with ethene adsorbed (π-bonded) on the $[GaH_2]^+Z_m^-$. Intermediate J indicates that the tetrahedral Ga species is coordinated with only one framework oxygen (monodentate). After the desorption of ethene, the $[GaH_2]^+$ species should relax to the more stable bidentate coordination (species K), as shown in Scheme 3.

Various energy terms for ethene desorption ($\Delta_{EA} E_a$, $\Delta_{EA} G_a^0$, $\Delta_{EA} E_r$ and $\Delta_{EA} G_r^0$) are reported in Table 3. Desorption of ethene from Ga–alkyl species has been well studied [33,41], and a very high activation barrier of about 60 kcal/mol has been reported. Because desorption is associated with the Ga species adjacent to a single-framework Al, the activation barrier is expected to be independent (structure insensitive) of the distance between the framework Al–pair. In the reminder of this section, we discuss the details of the alkyl activation mechanism for each catalytic site.

For the 4-membered ring cluster Z4a, the overall free energy of alkyl activation ($\Delta_A G_a^0$) is lower than the carbenium activation: 47.6 and 42.7 kcal/mol (Table 3) for alkyl activation, compared with 61.1 and 58.4 kcal/mol (Table 2) for carbenium activation. The free energies of activation for ethene removal are 62.0 and 64.4 kcal/mol, respectively.

The stability of the bicationic gallium monohydride species in the S5a ring makes alkyl activation more difficult compared with that for Z4a. As expected, the free energy activation barriers (66.4, 61.9, 66.6, and 54.7 kcal/mol) are lower than those for carbenium activation. The structure-insensitive ethene removal step faces typical free energy barriers of 56.5, 57.8, 48.8, and 63.9 kcal/mol.

The S6a structure has large free energy barriers ($\Delta_A G_a^0$) of 69.6 and 73.8 kcal/mol, with ethene removal barriers of 60.5 and 54.7 kcal/mol. The four alkyl activation pathways for the S6b site have free energy barriers ($\Delta_A G_a^0$) of 64.7, 67.9, 69.3, and 70.2 kcal/mol, with ethene removal barriers of ca. 62 kcal/mol.

The Z8a ring structure provides a less stable coordination for the $[GaH]^{2+}$ species, with lower resulting activation barriers for C–H dissociation by the alkyl activation mechanism. We calculated the free energy activation barriers to be 42.5 and 37.7 kcal/mol. Ethene removal barriers of 63.3 and 64.1 kcal/mol would make this the rate-limiting step.

For the least stable site, Z8b, the alkyl activation barriers ($\Delta_A G_a^0$) are 29.0 and 27.0 kcal/mol. The barriers for the formation of the undercoordinated GaH species are relatively higher. The ethene desorption barriers are 65.5 and 66.8 kcal/mol for this particular site. Thus, alkene desorption is a rate-limiting step for the overall alkyl activation catalytic cycle irrespective of the activity of the particular catalytic site. Recently, Pidko et al. [42] reported a novel one-step H_2 and C_2H_4 desorption pathway from gallium alkyl intermediate. This pathway involves a cyclic transition state with an activation barrier of 53.5 kcal/mol. We also calculated an activation barrier of 54.6 kcal/mol using a single-framework substitution model of the active site as described previously [33]. Thus, this mechanism of decomposition should set a lower limit of about 55 kcal/mol for the apparent activation barrier.

We repeated the calculation of this cyclic transition state for all the pair site models; the resulting activation energies ($\Delta_{\mathrm{ED}}E_{\mathrm{a}}$) are reported in Table 3. The constant values of $\Delta_{\mathrm{ED}}E_{\mathrm{a}}$ suggest that this decomposition mechanism is a structure-insensitive reaction.

3.3. *Hydrogen removal*

Carbenium activation or alkyl activation of an alkane leads to formation of the Brønsted acid site and the gallium dihydride as intermediates. To complete the catalytic cycle, it is essential to study the removal of molecular hydrogen (H_2) to regenerate the active site by combining the Brønsted proton and the hydridic hydrogen ($K \rightarrow L^{\ddagger} \rightarrow M \rightarrow N^{\ddagger} \rightarrow P \rightarrow A + H_2$), as shown in Schemes 2 and 3. The generalized mechanism starts with an adjustment of the coordination ($K \rightarrow L^{\ddagger} \rightarrow M$) of the $[GaH_2]^+$ species. Its coordination with the host zeolite changes from bidentate to tridentate. This adjustment occurs mainly to bring the Brønsted proton and the hydridic hydrogen closer to each other. A subsequent mechanistic step ($M \rightarrow N^{\ddagger} \rightarrow P$) leads to actual formation of the dihydrogen (H_2) molecule. In some cases, molecular hydrogen (H_2) remains adsorbed on the coordinatively unsaturated $[GaH]^{2+}$ species. Desorption of H_2 regenerates the active site, thereby completing dehydrogenation mechanism. Similar to carbenium and alkyl activation, for hydrogen removal we define overall activation energy ($\Delta_{\mathrm{H}}E_{\mathrm{a}}$) as the energy difference between the transition state $N^{\ddagger}$ and K. In the same way, we define the overall free energy of activation ($\Delta_{\mathrm{H}}G_{\mathrm{a}}^{0}$) to compare the rates between different mechanistic steps and identify the rate-limiting step. Table 4 reports the hydrogen removal free energy barriers for various ring structures that we have studied here.

For the Z4a ring structures, the transition states for hydrogen removal indicate that the hydrogen molecule is located far from the active site and does not coordinate directly with the coordinatively unsaturated Ga or the bridging oxygen. The transition state eigenvector mainly corresponds to the translational motion of the hydrogen molecule away from the site. The relaxation of this transition state ($N^{\ddagger}$) on the product side leads to the formation of the dihydrogen physisorbed (intermediate P in Scheme 2) on the coordinatively unsaturated GaH species. The free energy barrier for H_2 removal is 36.9 and 32.7 kcal/mol. For Z4a, the rate-limiting step for carbenium mechanism is the initial C–H dissociation, whereas the rate of the alkyl activation mechanism is limited by the ethene removal step.

We observed a very large variation in the hydrogen removal activation barrier for the S5a structure. We found free energy barriers ($\Delta_{\mathrm{H}}G_{\mathrm{a}}^{0}$) of 24.4, 49.0, 18.2, and 4.8 kcal/mol for the four reaction paths that we studied. A very high activation barrier for path 2 originates from the excess stability of the Brønsted proton located on the O05 bridging oxygen (Fig. 2). This is qualitatively in agreement with the rest of the results. From Table 1, it can be seen that the reduction is less endothermic, indicating that pathway 2 is the favored pathway for reduction. Correspondingly, the H_2 removal free energy barrier (reverse of the reduction process) is expected to be higher. For pathway 4, the hydrogen removal transition state ($N^{\ddagger}$) is stabilized by the coordination of the gallium monohydride species with three framework oxygen atoms. The resulting activation barrier of 4.8 kcal/mol is much lower.

Table 4
Energy barriers and reaction energies for the hydrogen removal step ($K \rightarrow N^{\ddagger} \rightarrow A + H_2$)

Cluster	Path	$K \rightarrow N^{\ddagger} \rightarrow A + H_2$			
		$\Delta_{\mathrm{H}}E_{\mathrm{a}}$	$\Delta_{\mathrm{H}}G_{\mathrm{a}}^{0}$	$\Delta_{\mathrm{H}}E_{\mathrm{r}}$	$\Delta_{\mathrm{H}}G_{\mathrm{r}}^{0}$
Z4a	1	37.2	36.9	6.1	0.1
	2	33.1	32.7	8.3	2.3
S5a	1	23.1	24.4	−24.0	−29.6
	2	48.6	49.0	−10.4	−15.9
	3	17.4	18.2	−23.2	−28.8
	4	3.6	4.8	−17.4	−23.3
S6a	1	15.5	16.3	−29.1	−35.3
	2	22.0	22.0	−31.5	−37.7
S6b	1	23.8	25.6	−19.9	−25.7
	2	26.5	28.2	−21.2	−26.5
	3	30.9	32.1	−21.0	−26.7
	4	24.9	26.4	−21.9	−27.5
Z8a	1	28.3	28.8	2.3	−3.8
	2	25.8	26.9	2.5	−3.6
Z8b	1	47.4	46.8	18.1	11.4
	2	33.6	33.8	17.2	10.4

Note: $\Delta_{\mathrm{H}}E_{\mathrm{a}}$, activation energy for H_2 removal; $\Delta_{\mathrm{H}}G_{\mathrm{a}}^{0}$, free energy barrier at STP for H_2 removal; $\Delta_{\mathrm{H}}E_{\mathrm{r}}$, reaction energy for H_2 removal; $\Delta_{\mathrm{H}}G_{\mathrm{r}}^{0}$, free energy change for H_2 removal reaction.

A very high stability of the $[GaH]^{2+}$ species in the six-membered ring naturally favors removal of the molecular hydrogen from intermediate K. The resulting free energy barriers for S6a structure are 16.3 and 22.0 kcal/mol. For the slightly less stable site S6b, the free energies of activation for hydrogen removal are 25.6, 28.2, 32.1, and 26.4 kcal/mol. Thus, for these sites, the rate-limiting step is either C–H activation or ethane removal.

As the gallium monohydride site becomes less stable compared with its reduced state, the activation barrier for hydrogen removal increases. This is evident from the higher free energy barriers (28.8 and 26.9 kcal/mol) for the Z8a site. For this particular site, we observed intermediate M, showing tridentate coordination of $[GaH]^{2+}$ species with framework oxygen atoms. After the molecular hydrogen forms, it remains adsorbed on the coordinatively unsaturated gallium.

For the least stable site, Z8b, the free energy barriers increase to 46.8 and 33.8 kcal/mol. The transition state structure ($N^{\ddagger}$) for the least stable site (Z8b) is similar to that of Z4a with similar activation barriers. The transition state eigenvector in $N^{\ddagger}$ corresponds to the translational motion of the dihydrogen toward the active site. This indicates that for less stable sites, the stabilization due to formation of the H–H bond is negated by the energy required for regeneration of the less stable Ga–monohydride site. Thus, if the reaction path is defined as the H–H distance, then the transition state lies farther along it. Eventually, movement of the dihydrogen away from the under-coordinated Ga itself becomes the significant activated process. For largely endothermic processes, similarity of the transition state to the products is expected.

3.4. *Reduction versus rearrangement of* $[GaH]^{2+}Z_d^{2-}$ *site*

Recently, Pidko et al. [42] claimed that the $[GaH]^{2+}Z_d^{2-}$ sites for larger Al–pair separations should rearrange by

$$[GaH]^{2+}Z_d^{2-} \leftrightarrow Ga^{+}Z_m^{-}–H^{+}Z_m^{-}. \qquad (2)$$

Thus, we have studied the same reaction for all of the pair–Al site reaction paths and plotted the resulting standard heat of rearrangement (ΔH^0_{rea}) against the heat of reduction (ΔH^0_{red}) as shown in Fig. 6. Similar to ΔH^0_{red}, ΔH^0_{rea} is endothermic ($\Delta H^0_{\text{rea}} > 0$) in most of the cases studied so far. This clearly indicates that the GaH sites in medium and small rings prefer to remain as $[GaH]^{2+}Z_d^{2-}$. The Y-intercept of the plot in Fig. 6 indicates that rearrangement is more endothermic by 7.3 kcal/mol compared with reduction. Thus in the presence of the hydrogen, the active sites are expected to undergo reduction rather than rearrangement.

Ethane dehydrogenation is a highly endothermic reaction ($\Delta E_{\text{r}} = 33.1$ kcal/mol), and the presence of the less stable intermediate along the optimum reaction path is expected. The traditional view of heterogeneous catalysis requires that the catalytic sites with well-defined structural and chemical form. However, if one accepts that a catalytic cycle has neither a start nor an end, then this strict requirement can be obviated. Naturally, the argument that catalytic site is more stable in some chemical forms compared with others becomes less important in such cases.

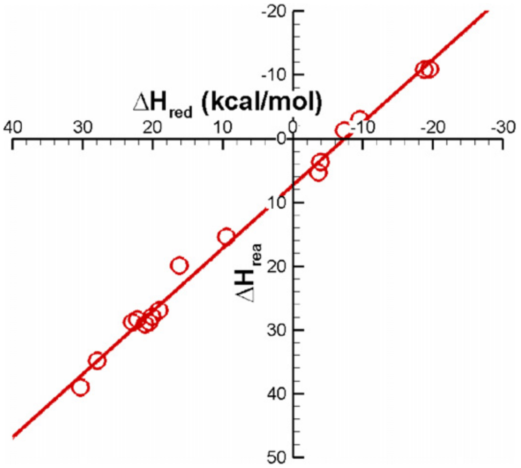

Fig. 6. Heat of rearrangement (ΔH^0_{rea}) plotted against heat of reduction (ΔH^0_{red}) for different catalytic sites.

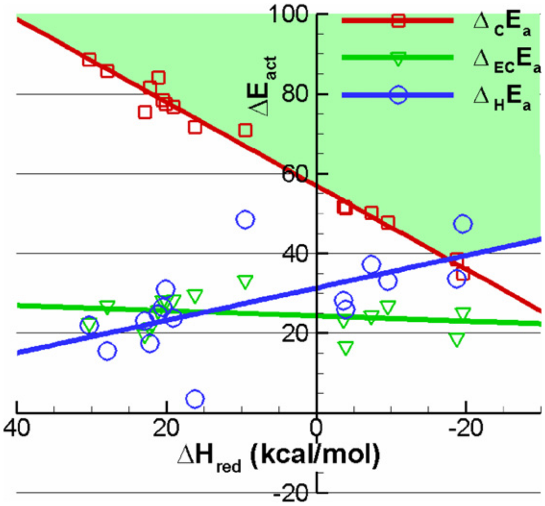

Fig. 7. Polanyi relations for catalytic dehydrogenation starting with carbenium activation—$\Delta_{\text{C}}E_{\text{a}}$ overall activation energy for C–H bond dissociation (red squares); $\Delta_{\text{EC}}E_{\text{a}}$ activation energy for ethene desorption from ethoxide (green triangles); $\Delta_{\text{H}}E_{\text{a}}$ overall activation energy for H_2 removal step (blue circles). Shaded region indicates possible value of apparent activation barrier. (For interpretation of the references to color in this figure legend, the reader is referred to the web version of this article.)

3.5. *Thermochemistry*

Our foregoing discussions clearly show that the stability of the catalytic site can be defined in terms of the heat of reduction (ΔH^0_{red}) of $[GaH]^{2+}Z_d^{2-}$ (Table 1). We find that the activity of the site, calculated in terms of the various energy barriers ($\Delta_{\text{C}}E_{\text{a}}$, $\Delta_{\text{A}}E_{\text{a}}$ and $\Delta_{\text{H}}E_{\text{a}}$), is strongly correlated with the stability of the active site. Fig. 7 plots the overall activation energies against the standard heats of reduction for the mechanistic steps of carbenium activation. Activation energy is plotted for (a) C–H dissociation by the carbenium mechanism, $\Delta_{\text{C}}E_{\text{a}}$; (b) ethene desorption, $\Delta_{\text{EC}}E_{\text{a}}$; and (c) hydrogen removal $\Delta_{\text{H}}E_{\text{a}}$. There is a clear correlation between the heat of reduction and the carbenium activation energy. The overall carbenium activation energy ($\Delta_{\text{C}}E_{\text{a}}$) decreases rapidly with decreasing (more exothermic) heat of reduction (ΔH^0_{red}). The less stable sites (Z4a, Z8a, and Z8b) show lower activation barriers. Ethene removal from an alkoxide intermediate, leaving behind the Brønsted acid site, results in an activation barrier of about 25 kcal/mol. This barrier decreases slightly with decreasing stability of the site. As the stability of the $[GaH]^{2+}Z_d^{2-}$ site decreases, the hydrogen removal barrier increases. We also see that the decrease in the carbenium activation barrier is much steeper than the gain in the hydrogen removal barrier. For C–H dissociation, the deviation from the linear correlation is lower ($R^2 = 0.98$) than that for H_2 removal ($R^2 = 0.37$). The flexibility of the Ga coordination in transition state $N^{\ddagger}$ (H_2 removal) compared with the transition state for carbenium activation ($E^{\ddagger}$) could explain both of these observations. These linear correlations are similar to the Brønsted–Evans–Polanyi relationships [47] proposed for homologous reaction families, which draw linear correlations between the activation barriers and the heats of the reactions. We note that both C–H dissociation and H_2 removal barriers are linearly correlated to the single parameter, ΔH^0_{red}. This phenomenon can be explained by the constant heat of reaction for the closed catalytic cycle of ethane dehydrogenation and the near-constant activation energy for the structure-insensitive ethene desorption. The lines corresponding to carbenium activation and hydrogen removal intersect at an activation energy (ordinate) of 38 kcal/mol.

Fig. 8 plots the overall activation energies against the heat of reduction for the alkyl activation. This plot includes (a) the overall activation energy for alkyl activation $\Delta_{\text{A}} E_{\text{a}}$; (b) the activation barrier for ethene desorption from $[\text{HGaC}_2\text{H}_5]^+$ species, $\Delta_{\text{EA}} E_{\text{a}}$; (c) the overall activation energy for H_2 removal, $\Delta_{\text{H}} E_{\text{a}}$; and (d) the activation energy for simultaneous desorption of ethene and H_2 via the cyclic transition state as proposed by Pidko et al. [42], $\Delta_{\text{ED}} E_{\text{a}}$. The H_2 removal barrier values are same irrespective of alkyl or carbenium activation. A linear Polanyi relation [47] between the overall alkyl activation barrier ($\Delta_{\text{A}} E_{\text{a}}$) and the heat of reduction (ΔH^0_{red}) is seen. The lines corresponding to alkyl activation and the hydrogen removal intersect at an activation energy value of 33 kcal/mol.

Comparing Figs. 7 and 8 leads to the following observations: (a) For the same heat of reduction, the alkyl activation barrier ($\Delta_{\text{A}} E_{\text{a}}$) is about 20 kcal/mol lower than the overall carbenium activation barrier ($\Delta_{\text{C}} E_{\text{a}}$); (b) the point of intersection of two lines is less sensitive to the accuracy of the calculation; and (c) despite the lower activation barrier for dissociation of the C–H bond, the rate-limiting step of alkene removal has an activation barrier of about 60 kcal/mol. For better visual understanding of the limitations on the apparent activation barrier, in Figs. 7 and 8, the regions of possible value of the apparent activation barrier are shaded. In Fig. 8 contains an additional line for the activation barrier ($\Delta_{\text{ED}} E_{\text{a}}$) proposed by Pidko et al. [42] for decomposition of the gallium–alkyl species. The activation barrier for such decomposition is structure-insensitive, which is evident from the zero slope of the Polanyi relation. The cyclic transition state provides the more facile path for decomposition of the Ga–alkyl species. However, the apparent activation barrier for the catalytic cycle for alkyl activation has a lower limit of 55 kcal/mol. The comparison clearly indicates that the carbenium activation mechanism is more facile dehydrogenation mechanism near the optimum region indicated by the cross-section of the two Polanyi relations. A highly facile alkyl activation along with highly activated alkene removal would mean that the gallium–alkyl species $[\text{HGaC}_2\text{H}_5]^+\text{Z}^-_m$ could be the "most abundant surface intermediate" (MASI). However, a high alkene removal barrier would indicate that it will be a "spectator species." A DRIFTS study by Kazansky et al. [26] revealed the presence of the $[\text{HGaC}_2\text{H}_5]^+$ species after the catalyst was heated in the presence of ethane.

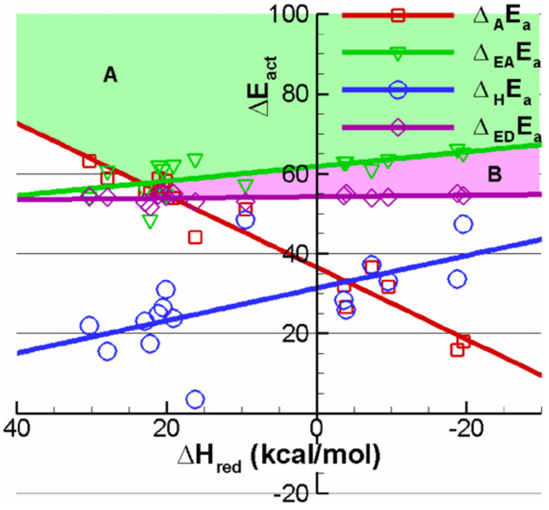

Fig. 8. Polanyi relations for catalytic dehydrogenation starting with alkyl activation—$\Delta_{\text{A}} E_{\text{a}}$ overall activation energy for C–H bond dissociation (red squares); $\Delta_{\text{EA}} E_{\text{a}}$ activation energy for ethene desorption from ethoxide (green triangles); $\Delta_{\text{H}} E_{\text{a}}$ overall activation energy for H_2 removal step (blue circles); $\Delta_{\text{ED}} E_{\text{a}}$ activation energy for Ga–alkyl species decomposition via cyclic transition state. (For interpretation of the references to color in this figure legend, the reader is referred to the web version of this article.) Shaded region A: Limits on the apparent activation energy for alkyl activation catalytic cycle as shown in Scheme 2. Shaded region B: Additional area for apparent activation barrier if decomposition via cyclic transition state as proposed by Pidko et al. [42].

As shown in Tables 2 and 3, the free energy barrier for mechanistic steps involving adsorption of the molecules is substantially greater than the activation energy, and these free energy changes are sensitive to temperature. Fig. 9 shows the free energy of reduction (ΔG_{red}) as a function of temperature for various reduction paths. For reduction by molecular hydrogen, overall entropy loss occurs, indicating that ΔS_{red} is < 0. With ΔS_{red} and ΔH_{red} almost constant, $\Delta G_{\text{red}}(\Delta G = \Delta H - T\Delta S)$ increases linearly with increasing temperature. Such reactions as propane aromatization are carried out at high temperatures (e.g., 800 K). Thus, Fig. 9 indicates that at actual reaction conditions, the free energy of reduction is positive for all sites, and the positive free energy change indicates that most of the pair sites will prefer to remain in the nonreduced state ($[\text{GaH}]^{2+}\text{Z}^{2-}_d$) at higher temperature. This result is equivalent to the decreasing surface coverage of the adsorbed species (in this case, hydrogen as a hydride or Brønsted acid site) with increasing temperature. Thus, high reaction temperatures should activate the catalyst by generating active sites with larger framework Al–pair distances.

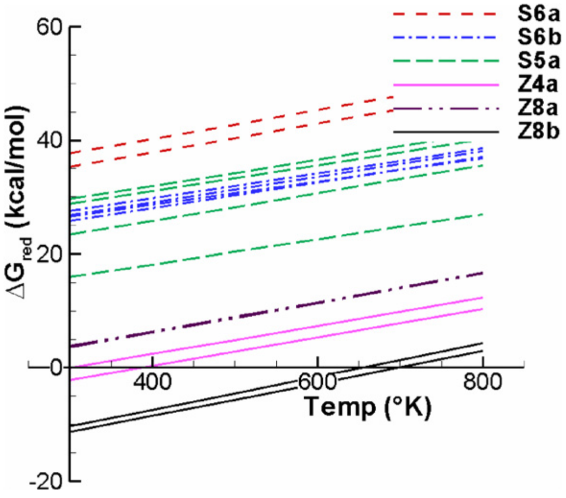

Fig. 9. Free energy of reduction (ΔG_{red}) as a function of temperature for different $[\text{GaH}]^{2+}\text{Z}^{2-}_d$ sites. Multiple lines correspond to multiple reduction paths for the same monohydride site.

Higher temperatures are also necessary to achieve favorable equilibrium for the highly endothermic dehydrogenation reaction. Although the Z4a, Z8a, and Z8b sites are less stable in the gallium–monohydride form at room temperature, under actual reaction conditions, they are stable with a positive free energy of reduction.

We carried out further investigations into the effect of reaction temperature on the free energy of activation. Fig. 10 shows the free energy for the carbenium activation mechanism ($\Delta_{\mathrm{C}}G_{\mathrm{a}}$, $\Delta_{\mathrm{H}}G_{\mathrm{a}}$) versus the free energy of reduction (ΔG_{red}) at three different temperatures (300, 550, and 800 K). Because carbenium activation and hydrogen removal are sequential steps of the dehydrogenation mechanism, the intersection of the two lines in this plot indicates an optimum site in terms of dehydrogenation activity. For such a site, carbenium dissociation and hydrogen removal activity will be balanced. As we noted above, the free energy of reduction increases with increasing temperature. Thus, both lines move to the left with increasing temperature, and the line corresponding to the carbenium dissociation moves upward due to the negative entropy change of the activated adsorption or C–H dissociation. With increasing temperature, the line corresponding to the H_2 removal moves slightly upward. Note that the abscissa and ordinate value of the intersection (free energy of reduction, $\Delta G_{\mathrm{red}}^{\mathrm{opt}}$, and free energy of activation, $\Delta G_{\mathrm{act}}^{\mathrm{opt}}$) remain approximately constant with increasing temperature. At higher temperature, the same free energy of reduction will correspond to a lower standard heat of reduction $\Delta H_{\mathrm{red}}^{0}$. This indicates that at higher temperature, the sites with lower $\Delta H_{\mathrm{red}}^{0}$ values (more exothermic and thus less stable) are the active dehydrogenation sites. This clearly indicates that the sites with larger Al–Al separation than those studied here (i.e., Z8b) will be important. This extrapolation will reduce the stringency of the requirement of Al–pairs in the small rings. In contrast, our study suggests that sites with smaller Al–Al distances are inactive at higher temperatures. Our analysis indicates that the optimum Al–Al distance will depend on the reaction conditions such as temperature, ethane partial pressure, and hydrogen partial pressure.

3.6. Si/Al ratio and dehydrogenation activity

Our thermochemical analysis suggests that at the reaction temperature, sites with greater Al–Al distances will be the active sites for dehydrogenation. This indicates that increasing the number of pair sites by decreasing the Si/Al ratio to a very low value (as in the case of Y zeolite) will not generate a catalyst with better activity. A very high framework–Al content will lead to formation of many $[\mathrm{GaH}]^{2+}$ sites stabilized by the small ring structure (5- or 6-membered). These sites will not be active for carrying out dehydrogenation due to their higher stability. Thus, high-silica zeolites such as ZSM-5 will be a better choice for providing large numbers of the pair–Al sites with optimum Al–Al distances. Kwak and Sachtler [21] have found that the maximum propane aromatization activity of Ga/HZSM-5 occurs at a Ga/Al ratio of about 0.5 (50% gallium exchange). Our finding that pair sites play important roles in

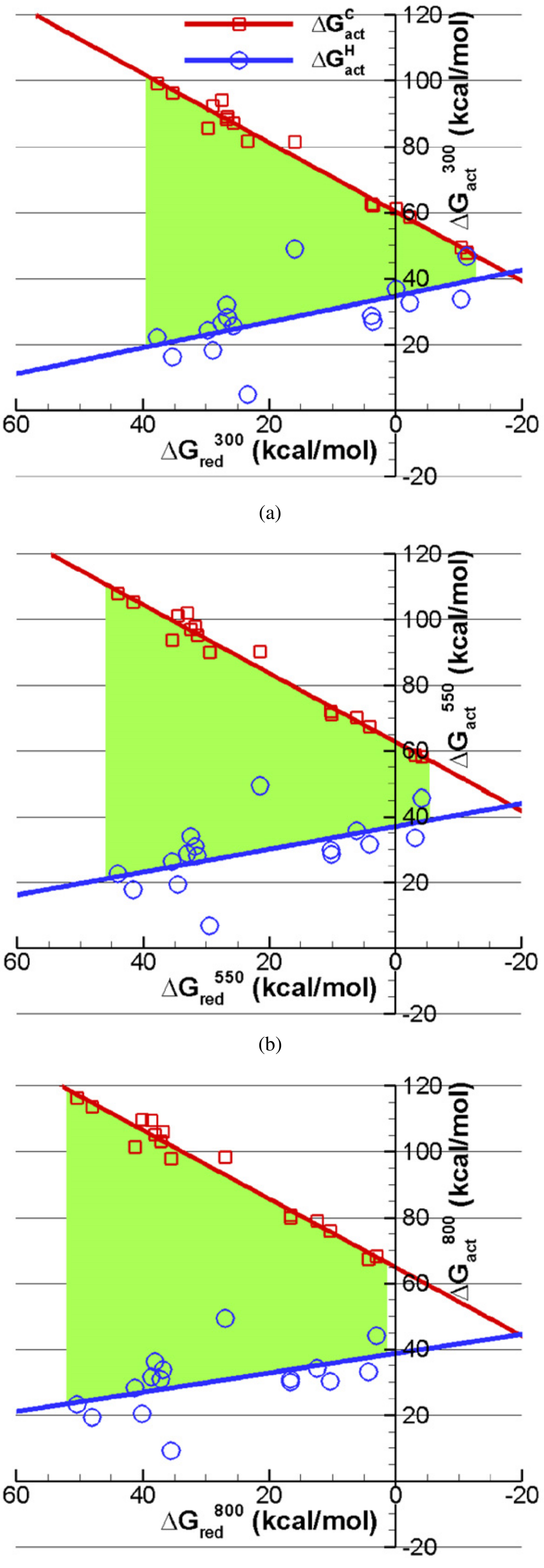

(a)

(b)

(c)

Fig. 10. ΔG_{act} vs ΔG_{red} for carbenium activation at three different temperature (a) 300, (b) 550, and (c) 800 K. In each plot $\Delta G_{\mathrm{act}}^{\mathrm{C}}$ overall activation energy for C–H bond dissociation (red squares); $\Delta G_{\mathrm{act}}^{\mathrm{H}}$ overall activation energy for H_2 removal step (blue circles). The green shaded region indicates the calculated values for the various active sites. (For interpretation of the references to color in this figure legend, the reader is referred to the web version of this article.)

dehydrogenation provides a simple rationale for such observations. Experimentally, it was found [24] that the propane aromatization faces a product inhibition by the molecular hydrogen. The higher hydrogen partial pressure will lead to reduction of the gallium–monohydride sites to form pairs of Brønsted acid sites and $[\mathrm{GaH_2}]^+\mathrm{Z}_m^-$. This will reduce the dehydrogenation activity, due simply to loss of the active dehydrogenation centers. This analysis indicates that these pair sites combining Brønsted acid site with a Lewis site ($\mathrm{GaH_2}$ cation) in fact could be the "portholes" for hydrogen removal from the surface, as proposed by Iglesia et al. [19].

3.7. Ga–H and O–H stretching frequencies

Table 5 reports Ga–H and O–H (Brønsted acid site) stretching frequencies, scaled by a factor of 0.9529 to account for anharmonic effects. Similar to our previous observation [33], the Ga–H frequencies for $[\mathrm{GaH}]^{2+}\mathrm{Z}_m^{2-}$ site are in good agreement with the DRIFTS [25,26] frequencies for Ga–H stretching. In fact, Ga–H frequencies for $[\mathrm{GaH_2}]^+\mathrm{Z}_d^-$ site are well below 2000 $\mathrm{cm^{-1}}$ to find any match. This again is a surprising result; the calculated frequencies are expected to be accurate to distinguish between two site types. However, neither the experimental nor the theoretical literature has a good explanation for this observation, and further investigation is needed.

4. Conclusion

Our study of the dehydrogenation activity of different $[\mathrm{GaH}]^{2+}\mathrm{Z}_d^{2-}$ sites in the zeolite provides strong theoretical evidence that pair–Al sites play important roles in the dehydrogenation reaction. We specifically compare the carbenium and alkyl pathways. Although alkyl activation is much more facile than the carbenium activation, ethene removal from $[\mathrm{HGaC_2H_5}]^+\mathrm{Z}_m^-$ intermediate faces a very high activation barrier of 60 kcal/mol. Thus, we conclude that this intermediate will be a spectator species while dominating the surface intermediates. This conclusion agrees well with recent experimental observations [26]. We find a linear Brønsted–Evans–Polanyi relation for such mechanistic steps as carbenium activation, alkyl activation, and hydrogen removal. We also find that with increasing distance between Al–Al, from a 6-membered ring to an 8-membered ring (S6a → S6b → Z8a → Z8b), the site's reduced stability is evident from the decreased heat of reduction ($\Delta H^0_{\mathrm{red}}$). Similarly, decreasing the distance from a 6-membered ring to a 4-membered ring (S6a → S5a → Z4a) causes loss of stability. The balance between activity and stability exemplifies the Sabatier principle for zeolite catalysis.

Our thermochemical analysis suggests that at reaction temperatures, most of the pair sites will be in their nonreduced form $[\mathrm{GaH}]^{2+}\mathrm{Z}_d^{2-}$. This suggests that high temperature not only aids endothermic dehydrogenation, but also increases the number of active sites in the catalyst (catalyst activation). Our thermochemical analysis has led us to conclude that under actual reaction conditions, the pair sites with larger Al–Al distances will play important roles. Thus, the structure of the optimum site will depend on the reaction temperature. The activity of such sites, measured in terms of the activation barrier, is less sensitive to temperature, however. The activation barrier for the optimum site (point of intersection of two Polanyi relations, $\Delta E^{\mathrm{opt}}_{\mathrm{act}}$) is 38.5 kcal/mol, in good agreement with the experimentally reported [44] activation barrier of 39 kcal/mol for ethane dehydrogenation. Increasing the distance between the framework–Al pair of the optimum site would mean that a higher fraction of the framework Al species would be able to form an active site.

Table 5
Scaled frequencies for Ga–H and O–H bonds in different catalytic site structures under consideration

Site	Ga–H[a]	Path	Ga–H[b]	Ga–H[b]	O–H[c]
Z4a	2082	1	1955	1974	3552
		2	1956	1982	3577
S5a	2075	1	1948	1970	3435
		2	1956	1979	3645
		3	1972	2004	3568
		4	1930	1998	3518
S6a	2075	1	1919	2001	3430
		2	1910	2001	3306
S6b	2077	1	1924	2014	3562
		2	1928	2002	3626
		3	1920	1994	3563
		4	1926	1987	3530
Z8a	2034	1	1929	2011	3568
		2	1934	1999	3542
Z8b	2068	1	1939	2013	3578
		2	1942	2009	3542

[a] Ga–H frequency in $\mathrm{cm^{-1}}$ for $[\mathrm{GaH}]^{2+}\mathrm{Z}_d^{2-}$ (intermediate A).

[b] Ga–H frequencies in $\mathrm{cm^{-1}}$ for $[\mathrm{GaH_2}]^+\mathrm{Z}_d^-$ (intermediate K).

[c] O–H frequencies for Brønsted acid site in the reduced site (intermediate K).

Acknowledgments

This work was supported by the State of Indiana through a grant from the 21st Century Technology Fund, US Department of Energy (DOE), Office of Basic Sciences (grant DE-FG02-03ER-15466) and the National Science Foundation (grant CTS-0238989-CAREER). Computational resources were obtained through a grant (MCA04N010) from the National Computational Science Alliance (Machines: copper.ncsa.uiuc.edu and tungsten.ncsa.uiuc.edu) and through supercomputing resources at Purdue University. The authors thank W. Nicholas Delgass and Gowri Krishnamurthy for helpful discussions on zeolite-catalyzed hydrocarbon chemistry.

Supporting information

Tables including important bond lengths and Mulliken charges of all structures for all 16 reaction pathways, along with detailed energetics of all reaction pathways. These 16 reaction pathways are Z4a (paths 1, 2), S5z (paths 1, 2, 3, 4), S6a (paths 1, 2), S6b (paths 1, 2, 3, 4), Z8a (paths 1, 2), and Z8b (paths 1, 2).

Please visit DOI:10.1016/j.jcat.2006.11.032.

References

[1] P.C. Doolan, P.R. Pujado, Hydrocarbon Process. 68 (1989) 72.
[2] N.S. Gnep, J.Y. Doyemont, A.M. Seco, F.R. Ribeiro, M. Guisnet, Appl. Catal. 43 (1988) 155.
[3] T. Mole, J.R. Anderson, G. Creer, Appl. Catal. 17 (1985) 127.
[4] W.O. Haag, R.M. Dessau, 8th International Congress on Catalysis, Berlin (West), 1984, p. 305.
[5] T.F. Narbeshuber, H. Vinek, J.A. Lercher, J. Catal. 157 (1995) 388.
[6] H. Kitagawa, Y. Sendoda, Y. Ono, J. Catal. 101 (1986) 12.
[7] R. Fricke, H. Kosslick, G. Lischke, M. Richter, Chem. Rev. 100 (2000) 2303.
[8] G.L. Price, V. Kanazirev, K.M. Dooley, V.I. Hart, J. Catal. 173 (1998) 17.
[9] M. Guisnet, N.S. Gnep, F. Alario, Appl. Catal. A 89 (1992) 1.
[10] G. Giannetto, R. Monque, R. Galiasso, Catal. Rev. Sci. Eng. 36 (1994) 271.
[11] Y. Ono, Catal. Rev. Sci. Eng. 34 (1992) 179.
[12] P. Meriaudeau, C. Naccache, J. Mol. Catal. 50 (1989) L7.
[13] N.S. Gnep, J.Y. Doyement, M. Guisnet, in: H.G. Karge, J. Weitkamp (Eds.), Zeolites as Catalysts, Sorbents and Detergent Builders, Elsevier, Amsterdam, 1989, p. 153.
[14] I. Takahara, M. Saito, M. Inaba, K. Murata, Catal. Lett. 96 (2004) 29.
[15] P. Meriaudeau, M. Primet, J. Mol. Catal. 61 (1990) 227.
[16] S.E. Collins, M.A. Baltanas, A.L. Bonivardi, Langmuir 21 (2005) 962.
[17] P. Meriaudeau, C. Naccache, J. Mol. Catal. 59 (1990) L31.
[18] J.A. Biscardi, E. Iglesia, Catal. Today 31 (1996) 207.
[19] E. Iglesia, D.G. Barton, J.A. Biscardi, M.J.L. Gines, S.L. Soled, Catal. Today 38 (1997) 339.
[20] N.S. Gnep, J.Y. Doyement, M. Guisnet, J. Mol. Catal. 45 (1988) 281.
[21] B.S. Kwak, W.M.H. Sachtler, J. Catal. 145 (1994) 456.
[22] R. Le Van Mao, L. Dufresne, Appl. Catal. 52 (1989) 1.
[23] G.L. Price, V. Kanazirev, J. Mol. Catal. 66 (1991) 115.
[24] G.D. Meitzner, E. Iglesia, J.E. Baumgartner, E.S. Huang, J. Catal. 140 (1993) 209.
[25] V.B. Kazansky, I.R. Subbotina, R.A. van Santen, E.J.M. Hensen, J. Catal. 227 (2004) 263.
[26] V.B. Kazansky, I.R. Subbotina, R.A. van Santen, E.J.M. Hensen, J. Catal. 233 (2005) 351.
[27] E.J.M. Hensen, M. Garcia-Sanchez, N. Rane, P.C.M.M. Magusin, P.-H. Liu, K.-J. Chao, R.A. van Santen, Catal. Lett. 101 (2005) 79.
[28] I. Nowak, J. Quartararo, E.G. Derouane, J.C. Vedrine, Appl. Catal. A 251 (2003) 107.
[29] A. Bhan, S.-H. Hsu, G. Blau, J.M. Caruthers, V. Venkatasubramanian, W.N. Delgass, J. Catal. 235 (2005) 35.
[30] A. Bhan, Y.V. Joshi, W.N. Delgass, K.T. Thomson, J. Phys. Chem. B 107 (2003) 10476.
[31] Y.V. Joshi, A. Bhan, K.T. Thomson, J. Phys. Chem. B 108 (2004) 971.
[32] Y.V. Joshi, K.T. Thomson, J. Catal. 230 (2005) 440.
[33] Y.V. Joshi, K.T. Thomson, Catal. Today 105 (2005) 106.
[34] E.A. Furtado, I. Milas, J. Lins, M.A.C. Nascimento, Phys. Status Solidi A 187 (2001) 275.
[35] I. Milas, M.A.C. Nascimento, Chem. Phys. Lett. 338 (2001) 67.
[36] M.R.S. Pereira, M.A.C. Nascimento, Theor. Chim. Acta 110 (2003) 441.
[37] H. Himei, M. Yamadaya, M. Kubo, R. Vetrivel, E. Broclawik, A. Miyamoto, J. Phys. Chem. 99 (1995) 12461.
[38] E. Broclawik, H. Himei, M. Yamadaya, M. Kubo, A. Miyamoto, R. Vetrivel, J. Chem. Phys. 103 (1995) 2102.
[39] N.O. Gonzales, A.K. Chakraborty, A.T. Bell, Top. Catal. 9 (1999) 207.
[40] I. Kuzmin, G. Zhidomirov, E. Hensen, Catal. Lett. 108 (2006) 187.
[41] M.V. Frash, R.A. van Santen, J. Phys. Chem. A 104 (2000) 2468.
[42] E.A. Pidko, V.B. Kazansky, E.J.M. Hensen, R.A. van Santen, J. Catal. 240 (2006) 73.
[43] N. Rane, A.R. Overweg, V.B. Kazansky, R.A. van Santen, E.J.M. Hensen, J. Catal. 239 (2006) 478.
[44] J. Bandiera, Y.B. Taarit, Appl. Catal. A 152 (1997) 43.
[45] M.S. Pereira, M.A.C. Nascimento, Chem. Phys. Lett. 406 (2005) 446.
[46] X. Rozanska, M. Garcia-Sanchez, E.J.M. Hensen, R.A. Van Santen, C. R. Chimie 8 (2005) 509.
[47] M.G. Evans, M. Polanyi, Trans. Faraday Soc. 34 (1938) 11.
[48] L.A.M.M. Barbosa, R.A. van Santen, J. Hafner, J. Am. Chem. Soc. 123 (2001) 4530.
[49] A.A. Shubin, G.M. Zhidomirov, V.B. Kazansky, R.A. van Santen, Catal. Lett. 90 (2003) 137.
[50] L. Barbosa, R.A. van Santen, J. Phys. Chem. B 107 (2003) 14342.
[51] L. Benco, T. Bucko, J. Hafner, H. Toulhoat, J. Phys. Chem. B 108 (2004) 13656.
[52] L. Benco, T. Bucko, J. Hafner, H. Toulhoat, J. Phys. Chem. B 109 (2005) 20361.
[53] V.B. Kazansky, I.R. Subbotina, N. Rane, R.A. van Santen, E.J.M. Hensen, Phys. Chem. Chem. Phys. 7 (2005) 3088.
[54] H.V. Koningsveld, H.V. Bekkum, J.C. Jansen, Acta Crystallogr. Sect. B Struct. Sci. B 43 (1987) 127.
[55] M.J. Rice, A.K. Chakraborty, A.T. Bell, J. Phys. Chem. B 104 (2000) 9987.
[56] A.T. Bell, in: G. Centi, A.T. Bell, B. Wichterlova (Eds.), Catalysis by Unique Metal Ion Structures in Solid Matrices: From Science to Application, Kluwer Academic, Dordrecht, 2001, p. 331.
[57] W. Loewenstein, Am. Mineral. 39 (1954) 92.
[58] A.D. Becke, J. Chem. Phys. 98 (1993) 5648.
[59] C. Lee, W. Yang, R.G. Parr, Phys. Rev. B Condens. Matter 37 (1988) 785.
[60] M.M. Francl, W.J. Pietro, W.J. Hehre, J.S. Binkley, M.S. Gordon, D.J. DeFrees, J.A. Pople, J. Chem. Phys. 77 (1982) 3654.
[61] M.J. Frisch, G.W. Trucks, H.B. Schlegel, G.E. Scuseria, M.A. Robb, J.R. Cheeseman, J.A. Montgomery Jr., T. Vreven, K.N. Kudin, J.C. Burant, J.M. Millam, S.S. Iyengar, J. Tomasi, V. Barone, B. Mennucci, M. Cossi, G. Scalmani, N. Rega, G.A. Petersson, H. Nakatsuji, M. Hada, M. Ehara, K. Toyota, R. Fukuda, J. Hasegawa, M. Ishida, T. Nakajima, Y. Honda, O. Kitao, H. Nakai, M. Klene, X. Li, J.E. Knox, H.P. Hratchian, J.B. Cross, C. Adamo, J. Jaramillo, R. Gomperts, R.E. Stratmann, O. Yazyev, A.J. Austin, R. Cammi, C. Pomelli, J.W. Ochterski, P.Y. Ayala, K. Morokuma, G.A. Voth, P. Salvador, J.J. Dannenberg, V.G. Zakrzewski, S. Dapprich, A.D. Daniels, M.C. Strain, O. Farkas, D.K. Malick, A.D. Rabuck, K. Raghavachari, J.B. Foresman, J.V. Ortiz, Q. Cui, A.G. Baboul, S. Clifford, J. Cioslowski, B.B. Stefanov, G. Liu, A. Liashenko, P. Piskorz, I. Komaromi, R.L. Martin, D.J. Fox, T. Keith, M.A. Al-Laham, C.Y. Peng, A. Nanayakkara, M. Challacombe, P.M.W. Gill, B. Johnson, W. Chen, M.W. Wong, C. Gonzalez, J.A. Pople, Gaussian03, Revision B.5, Gaussian, Inc., Pittsburgh PA, 2003.
[62] M. Sierka, J. Sauer, J. Phys. Chem. B 105 (2001) 1603.